Composite Structures 345 (2024) 118406

Contents lists available at ScienceDirect

Composite Structures

journal homepage: www.elsevier.com/locate/compstruct

Theoretical study on the bond performance of CFRP-to-steel single-lap shear tests with multiple debonding defects

Hugo C. Biscaia [a,b,*], Pedro Coelho [a,b], Fábio Conde [a,b], Tommaso D'Antino [c]

[a] UNIDEMI, Department of Mechanical and Industrial Engineering, NOVA School of Science and Technology, 2829-516 Caparica, Portugal
[b] Laboratório Associado de Sistemas Inteligentes, LASI, 4800-058 Guimarães, Portugal
[c] Department of Architecture, Built Environment, and Construction Engineering (ABC), Politecnico di Milano, Milan, Italy

ARTICLE INFO

Keywords:
Debonding defects
Single-lap shear test
Bond-slip
CFRP-to-steel joints
Numerical simulation

ABSTRACT

The amount of research on the external bonding of Carbon Fiber Reinforced Polymers (CFRP) to degraded structures has increased recently. The adhesive is the weakest element of the joint and the bonding of the adherends is critical for the efficiency of the joint. Therefore, the influence of multiple debonding defects on CFRP-to-steel joints has still not been correctly quantified nor fully understood. For this reason, the current work proposes a new numerical strategy that allows for studying the influence of multiple debonding defects when a brittle and ductile adhesive is used. A new nonlinear bond-slip relationship is used and four different ratios between the debonded and the bonded area (η) are assumed: 0%, 25%, 50%, and 75%. The proposed model is based on the Finite Difference Method (FDM) and validation is carried out with a commercial Finite Element Method (FEM) package. The load-slip curves allowed for observing that the proposed FDM and the FEM are consistent and both revealed degradation of the load capacity of the joints with the increase of η. Moreover, by adopting a displacement control at the CFRP-free end, a snap-through and snap-back phenomenon are observed in the specimens with a localized debonding defect.

1. Introduction

The use of Carbon Fiber Reinforced Polymers (CFRP) to strengthen existing damaged structures has become a common technique mainly due to the recent increase in knowledge about the bond behaviour of CFRP-to-substrate joints. However, some main drawbacks of these bonding systems are well-known in the literature [1–8]. One of them that concerns researchers around the world is the premature debonding of the CFRP from the substrate, which means that the debonding occurs at a CFRP strain value lower than the rupture value. To mitigate or even avoid this issue several authors have experimentally [9–11] and/or numerically [12–14] studied different anchorage systems. However, the bond behaviour of a CFRP-to-substrate joint can be influenced by several factors that are described in the literature thoroughly, e.g. [7,15–17]. All these factors are based the hypothesis that the bond between adherends (CFRP and substrate) is perfect. Still, several defects that may affect the interfacial behaviour between the FRP composite and the substrate are associated with adhesively bonded structures such as kissing bonds, disbonds, delamination, cracks, air voids, porosity, poor cure, insufficient filling, adherend defects, irregular fillet geometry, and variation in bond line thickness [18]. All these defect types are hard to quantify either in terms of their position, shape or size, which causes high variability in the mechanical performance of FRP-to-steel joints. In addition, the construction process or the joint type can also make it difficult to identify imperfect interfaces. Thus, tubular [19–22], curved bonded joints [23–26] or, despite flat, stepped-lap bonded joints [27–29] are some examples of those cases that have bond areas with difficult access or, due to their inherent geometry, where it is difficult to fully control the bonding process of the adherends, e.g. keeping the adhesive thickness constant in the joint.

Although air voids can be controlled by careful design and/or application, the primary sources of porosity in adhesives are volatiles, entrapped air, and chemically originated due to reactions in their curing process [18]. Usually, adhesives are bi-component materials with Part A and Part B (resin and hardener, respectively) and poor mixing can cause air to be trapped in the adhesive. A careful bonding process of the adherends is also important since, for instance, if the setup is moved before the complete cure of the adhesive, air voids can be created in the adhesive [18]. The curing condition of adhesives is another aspect to take into account. Thus, different adhesives need to follow a particular

* Corresponding author.
E-mail address: hb@fct.unl.pt (H.C. Biscaia).

https://doi.org/10.1016/j.compstruct.2024.118406
Received 29 April 2024; Received in revised form 2 July 2024; Accepted 17 July 2024
Available online 20 July 2024

curing condition such as controlled temperature, pressure or light to achieve a good final cure. Otherwise, the curing process might not be carried out uniformly, which results in partially cured adhesives with a reduced final strength. These partially cured adhesives are more prone to crack and/or induce adhesive failures, which directly influences the bond performance of adhesively bonded structures negatively.

Therefore, when the CFRP composite is inadequately bonded onto the substrate, the bond performance of the CFRP-to-substrate joint will be affected. Under such circumstances, the issue that needs to be addressed urgently is that of quantifying the load degradation of the joint due to poor bonding, i.e. in the presence of multiple debonding defects. In such cases, two situations may be distinguished. The first corresponds to a defect where, for instance, air voids or superficial cracks are perfectly localized and concentrated within a region or regions throughout the bonded length whereas the second corresponds to a defect where the air voids are dispersed throughout the bonded area. To the best of our knowledge, although the same debonded area defect can be initially considered, the identification of the worst scenario, i.e. localized or dispersed, is not clarified yet and this doubt requires clarification. In this regard, Li et al. [30] carried out an experimental work on CFRP sheets externally bonded to concrete. The layouts considered by Li et al. [30] covered either localized or dispersed debonding defects and the specimens were tested under the pull–push single-lap direct shear test configuration. Different localizations and debonded areas were also considered. The results showed that an initial debonded area of 5 % of the total area led to marginal load degradations of the CFRP-to-concrete joints. The authors [30] also observed that the localized debonding defect led to higher load degradations than those obtained from the equivalent specimens (i.e. with the same initial debonded area) with a dispersed debonding pattern.

In another experimental study carried out by Wan et al. [31], also focusing on CFRP-to-concrete bonded joints, the debonding defects were created by carving grooves into the concrete surface. To avoid the bonding between the adhesive and the CFRP composite, the grooves were filled with soft sealant and Teflon. The results showed that crack widths larger than 3 mm in the concrete were prejudicial for the bond strength and fracture energy of the structure since both decreased as the debonding defects increased. However, under the presence of small defects, i.e. with groove widths lower than 1 mm, the CFRP-to-concrete interface increases its load capacity due to a redistribution of the bond stresses within the interface.

To mitigate all these aspects and even improve the bond between adherends, additional strategies are usually implemented. For instance, the surface preparation of the adherends is a popular topic of discussion among researchers [32–35]; the aim is to create irregular surfaces and slightly increase the bonded area. Therefore, friction forces can develop and small regions under compression can be created in the adhesive even when subjected to a pure shear load. Consequently, the final bond behaviour of the joint can be improved by increasing the maximum bond stresses developed within the interface between adherends.

Another topic that requires investigation is the type of adhesives used. Using brittle or ductile adhesives may affect the CFRP-to-substrate interface with more or less severity. Since in both cases the local bond behaviour shows different shapes, this also has a direct influence on the bond performance of the joint. In the case of a brittle adhesive, the CFRP-to-steel bonded joints are characterized by triangular bond-slip relationships [36–38], whereas trapezoidal bond-slip relationships are known to be a better representation of the local bond behaviour of CFRP-to-steel joints built with a ductile adhesive [39–41]. Compared with the triangular shape, the trapezoidal bond-slip relationship has a higher final slip (s_f), i.e. a slip beyond which no further bond stresses can be transferred between adherends and no more contact between them is ensured. Consequently, the effective bond length (L_{eff}) of these CFRP-to-steel joints, i.e., the minimum bonded length needed to fully establish the bond stress transfer mechanism, tends to be higher than those with triangular bond-slip relationship [42].

To answer these and other questions, the present work introduces a new numerical approach based on the Finite Difference Method (FDM), which considers multiple debonding defects throughout the bonded area. To facilitate the study with brittle and ductile adhesives a new nonlinear and single-function bond-slip relationship is proposed. This bond-slip relationship can locally represent different bonded joints under pure fracture mechanics Mode II condition and it can easily be adapted to the case of a residual bond stress in the presence of friction or peeling stresses. The proposed FDM is also validated by the Finite Element Method (FEM) and as a reference, the full bonding of the CFRP-to-steel joints, i.e. free of any initial debonding defects, is considered. To understand the influence of the multiple debonding defects on the bonded area and their various impacts on the effective bond length of the CFRP-to-steel joints, four different bonded lengths were also considered as well as localized and dispersed air voids throughout the bonded length. The results revealed that the specimens with the shortest bonded lengths are less sensitive to the type of debonding defect, whether localized or dispersed. However, for CFRP-to-steel joints with longer bonded lengths, less sensitivity to localized debonding defect was observed and the load degradation of these joints was almost kept unchanged. On the other hand, the specimens with dispersed debonding defects reached a maximum load degradation of approximately 24 % when compared with the corresponding reference specimens independently of the adhesive type.

2. Theoretical model

To facilitate the comprehension of the bond performance of FRP-to-substrate single-lap shear tests with multiple defects, this section presents the theoretical derivations and numerical strategy followed in this work. The single-lap shear test subjected to a monotonic load is reproduced and the initial assumptions considered in this work are provided.

2.1. Initial basic assumptions

The full debonding process between adherends such as an FRP composite and a substrate with multiple bond defects is based on some main initial assumptions that allow for deriving several equations and implementing a numerical strategy. So, along with the proposed theoretical modelling, the following six main bullet points should be kept in mind:

(i) Independently of the load transmitted to the reinforcement, an FRP composite with a linear elastic behaviour until failure is herein considered. Its initial thickness and width will remain constant during the full debonding process of the joint;
(ii) Normal deformations of the interface, i.e., those perpendicular to the bonded area, responsible for originating peeling stresses can be ignored when compared with the shear deformations, i.e., within the plane of the bonded area. Therefore, only the deformations consistent with Mode II are considered, which means that the bonded joint is under a pure fracture mechanics Mode II condition.
(iii) Each single point of the bonded area has the same local bond behaviour, which combines the bond stresses and the relative displacements between adherends (i.e. FRP composite and steel substrate), usually designated in the literature as a bond-slip relationship, e.g. [43–49]. As will be seen later, a novel and nonlinear single-function bond-slip relationship that can locally represent the bond behaviour of several bonded joints under different conditions is considered;
(iv) Across the width of the reinforcement a constant bond stress distribution is assumed. However, it should be noted that in the regions where the reinforcement has a debonding defect, no bond stresses are considered at that region and consequently, a bond

stress discontinuity will occur at the transitions between those bonded and debonded defect regions;

(v) Except for the finite elements with a fully debonding defect across the reinforcement width, a smeared debonding defect is associated with the finite element across the reinforcement width;

(vi) The yielding of the steel is not considered. Although the yielding strain of the steel can be controlled in the proposed FDM, this value was never reached. Otherwise, the yielding of the steel would be predicted during the debonding process of the CFRP-to-steel joints instead of the complete debonding of the FRP composite from the steel substrate.

2.2. Equilibrium conditions

To define the bond behaviour between a reinforcement such as an FRP composite externally bonded to a substrate subjected to a single-lap shear test, the finite segment dx shown in Fig. 1 is considered. Thus isolating the reinforcement from the substrate, the equilibrium of the horizontal forces leads to:

$$\frac{d\sigma_r}{dx} - \frac{\tau_b \cdot b_a}{t_r \cdot b_r} = 0 \tag{1}$$

whereas the following equation can be derived when only the substrate is considered:

$$\frac{d\sigma_s}{dx} + \frac{\tau_b \cdot b_a}{t_s \cdot b_s} = 0 \tag{2}$$

where σ_r and σ_s are the axial stress in the reinforcement and substrate, respectively; t_r and t_s are the thicknesses of the reinforcement and substrate, respectively; b_r and b_s are the widths of the reinforcement and substrate, respectively; b_a is the width of the reinforcement effectively bonded to the substrate; and τ_b is the bond stress locally developed within the bonded interface.

In addition, the sums of the forces acting in the reinforcement and the substrate are zero, i.e.:

$$\sigma_r \cdot A_r + \sigma_s \cdot A_s = 0 \tag{3}$$

where A_r and A_s are, respectively, the cross-sectional areas of the reinforcement and the substrate.

2.3. Governing equation

To obtain the governing equation of the debonding problem, firstly, the slip is defined as the relative displacement between adherends, reinforcement and substrate, i.e.:

$$s = u_r - u_s \tag{4}$$

where u_r and u_s are, respectively, the displacements of the reinforcement and the substrate. Assuming an elastic behaviour, the second derivative with respect to x of Eq. (4) allows us to write the following equations:

$$\frac{d\sigma_r}{dx} = E_r \cdot \left(\frac{d^2 s}{dx^2} + \frac{d^2 u_s}{dx^2} \right) \tag{5}$$

and

$$\frac{d\sigma_s}{dx} = E_s \cdot \left(\frac{d^2 u_r}{dx^2} - \frac{d^2 s}{dx^2} \right) \tag{6}$$

where E_r and E_s are the elastic modulus of the reinforcement and substrate, respectively. Combining Eq. (5) with Eq. (1) and Eq. (6) with Eq. (2) leads to:

$$\frac{d^2 s}{dx^2} + \frac{d^2 u_s}{dx^2} - \frac{\tau_b \cdot b_a}{E_r \cdot A_r} = 0 \tag{7}$$

and

$$\frac{d^2 s}{dx^2} - \frac{d^2 u_r}{dx^2} + \frac{\tau_b \cdot b_a}{E_s \cdot A_s} = 0 \tag{8}$$

From the second derivative of Eq. (4) with respect to x , Eq. (8) can be rewritten as:

$$\frac{d^2 u_s}{dx^2} - \frac{\tau_b \cdot b_a}{E_s \cdot A_s} = 0 \tag{9}$$

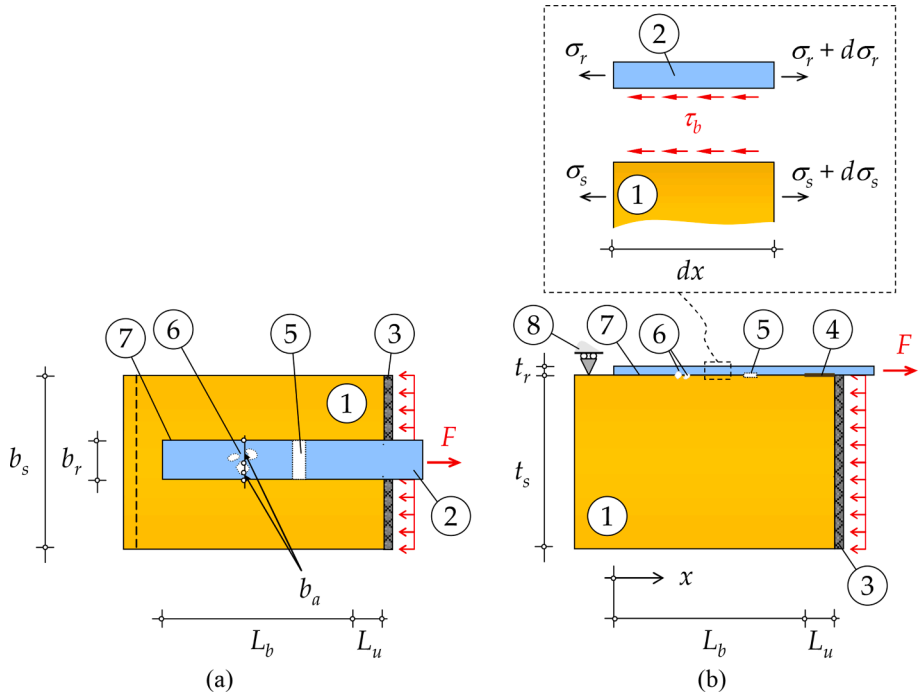

Fig. 1. Setup considered to derive the equilibrium conditions of an FRP composite externally bonded onto a substrate: (a) top view; and (b) side view.

By introducing Eq. (9) into Eq. (7), the following 2nd-order differential equation is obtained:

$$\frac{d^2s}{dx^2} - \lambda \cdot \tau_b = 0 \tag{10}$$

where

$$\lambda = b_a \cdot \left(\frac{1}{E_r \cdot A_r} + \frac{1}{E_s \cdot A_s} \right) \tag{11}$$

The result obtained in Eq. (11) is directly dependent on the width of the reinforcement effectively bonded to the substrate (b_a) and if this width is considered fully bonded to the substrate, then $b_a = b_r$ and Eq. (11) can be rewritten as:

$$\lambda = \frac{1}{E_r \cdot t_r} + \frac{b_r}{E_s \cdot A_s} \tag{12}$$

which is a well-known parameter used to describe the debonding process of an FRP composite from a substrate [50–55].

2.4. Local bond behaviour

To describe the local bond behaviour of an FRP externally bonded onto a substrate, it is usually mentioned in the literature that the type of substrate (e.g. concrete, timber, or steel) [56], the type of adhesive (e.g. brittle or ductile) [36–41], or the influence of external forces (e.g. due to a mechanical anchorage system) [57], may change the shape of the bond-slip relationship. Therefore, to accommodate all these aspects into a single-function bond-slip relationship, the following formula is proposed:

$$\frac{\tau_b(s)}{\beta \cdot \tau_{b\max}} = \left(1 - e^{-b \cdot s}\right) \cdot \frac{\frac{\alpha}{\beta} + e^{-a \cdot (s - s_t)}}{1 + e^{-a \cdot (s - s_t)}} \tag{13}$$

where a and b are parameters that should be determined by best fitting experimental data; s_t is the slip corresponding to the midpoint of the transition between the maximum ($\tau_{b\max}$) and the residual friction (τ_{bf}) stresses; β is a dimensionless parameter that is used to ensure that the maximum bond stress is reached and it can be obtained by a simple trial and error process; and α is the ratio between the residual and the maximum bond stresses defined as:

$$\alpha = \frac{\tau_{bf}}{\tau_{b\max}} \tag{14}$$

The versatility of this bond-slip relationship is shown in Fig. 2 in which several local bond behaviours of different bonded interfaces are represented. In all these, a certain number of stages can be seen. For instance, in the cases shown in Fig. 2a, 2c, and 2d, the following stages can be identified: (i) Elastic (E); (ii) Softening (S); Debonding (D), whereas in the cases shown in Fig. 2b and 2f the D stage is replaced by a Friction (F) stage. Only in the bond-slip relationship shown in Fig. 2e a Constant (C) stage between the E and the S stages can be observed.

All bond-slip relationships have an initial E stage, which is characterized by an increase in the bond stresses with the increase of the slips and it is denoted as the Elastic (E) stage. The E stage is assumed to end when the maximum bond stress ($\tau_{b\max}$) is reached. Based on the experimental data, the E stage has a smooth trend and for simplification, several authors have approximated it to a single power function [58–60] or a linear followed by a power function [61–63]. In this second case, the initial stiffness of the first branch tends to decrease in the second branch with the slip increase.

After the end of the E stage, two possibles paths can develop: the S or the C stage. The C stage is associated with ductile adhesives and is characterized by the same bond stresses with the increase of the slips. This stage ends when the bond stresses begin to decrease with the slips, i.e. when the S stage begins. Hence, the S stage is characterized by the development of bond stresses that decrease with the increase of the slips. In the absence of friction between adherends, the S stage ends at zero bond stress. From hereafter, no further bond stresses are being transferred and the D stage is reached. However, in the presence of compressive stresses originating, for instance, from compression forces applied by a mechanical anchorage, the S stage does not end with zero bond stress. Otherwise, the F stage, which is characterized by constant bond stress, appears mainly due to dry friction developed between the adherends and denoted as a frictional (or residual) stress (τ_{bf}). The value of τ_{bf} is as high as the friction between adherends, which can be justified by Coulomb's friction law, as discussed by some authors in the literature, e.g. [57,64,65].

Introducing Eq. (13) into Eq. (10), the following 2nd-order

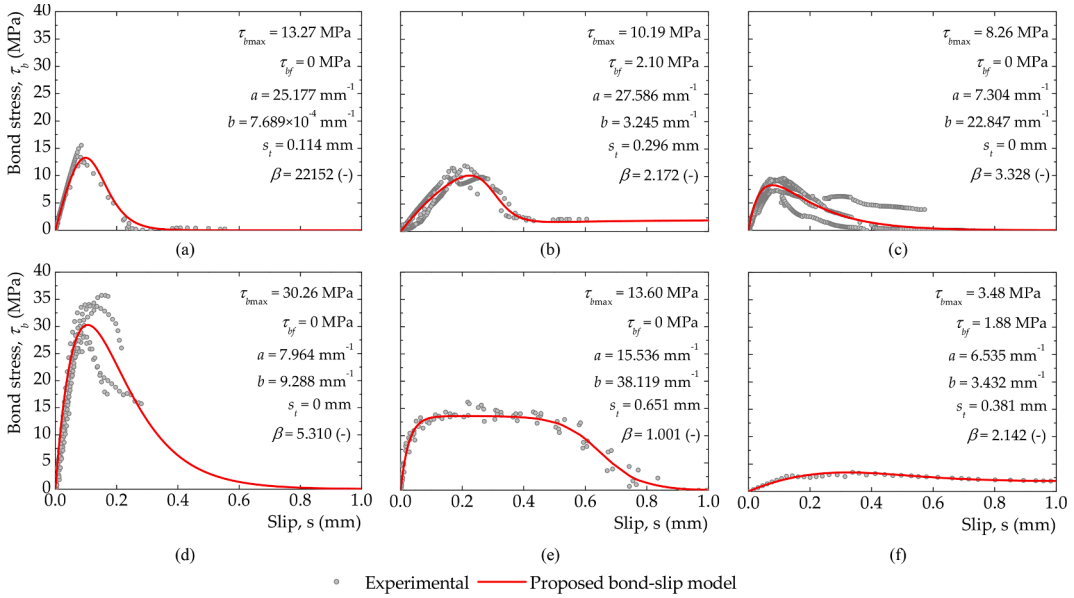

Fig. 2. Comparisons between the bond-slip relationship for different bonded interfaces: (a) CFRP-to-steel [56]; (b) CFRP-to-timber [56]; (c) CFRP-to-concrete [56]; (d) CFRP-to-steel with a brittle adhesive [66]; (e) CFRP-to-steel with a ductile adhesive [67]; (f) FRP-to-concrete with the influence of an external force with different magnitudes [68].

differential equation is obtained:

$$\frac{d^2s}{dx^2} - \lambda \cdot \beta \cdot \tau_{bmax} \cdot \left(1 - e^{-b \cdot s}\right) \cdot \frac{\frac{a}{\beta} + e^{-a \cdot (s - s_t)}}{1 + e^{-a \cdot (s - s_t)}} = 0 \tag{15}$$

For a constant value of λ, the analytical solution of Eq. (15) is not yet known. In addition, in this study, the parameter λ may vary with x , depending on the defects of the bonded interface, in the direction of the bonded length of the joint. For these reasons, a numerical strategy based on the Finite Difference Method (FDM) was implemented to obtain an approximated solution of Eq. (15). In the following subsection, the numerical strategy followed in the current work is explained in detail.

2.5. Proposed numerical strategy

As mentioned, the solution of Eq. (15) is obtained by implementing the FDM. Thus, the length of the reinforcement externally bonded to the substrate is discretized into equidistant n points and a regular step (h) is defined as:

$$h = \frac{L_b}{n} \tag{16}$$

where L_b is the bonded length of the reinforcement (see Fig. 3). The following approximations are used:

$$\frac{ds(x_i)}{dx} \approx \frac{s_{i+1} - s_{i-1}}{2h} \text{ for } i = 0, 1, 2, \ldots, n \tag{17}$$

and

$$\frac{d^2s(x_i)}{d^2x} \approx \frac{s_{i+1} - 2s_i + s_{i-1}}{h^2} \text{ for } i = 0, 1, 2, \ldots, n \tag{18}$$

Due to the nonlinearity of the generated system of equations, the solution is found by implementing the Newton-Raphson iterative technique defined as:

$$\{s_i\}_{j+1} = \{s_i\}_j - [J(s_i)]^{-1} \cdot \{f_i(s_i)\} \tag{19}$$

where $\{f_i(s_i)\}$ is the left-hand side of Eq. (15) at point i; $\{s_i\}_{j+1}$ and $\{s_i\}_j$ are the slips at each discretized point of the bonded length in the $j+1$-th and j-th iterations, respectively; and $[J(s_i)]^{-1}$ is the inverse of the Jacobian matrix defined as follows:

$$[J(s_i)] = \begin{bmatrix} \frac{\partial f_0(s_0, s_1)}{\partial s_0} & \frac{\partial f_0(s_0, s_1)}{\partial s_1} & \frac{\partial f_0(s_0, s_1)}{\partial s_2} & \cdots & \frac{\partial f_0(s_0, s_1)}{\partial s_{n-1}} \\ \frac{\partial f_1(s_0, s_1, s_2)}{\partial s_0} & \frac{\partial f_1(s_0, s_1, s_2)}{\partial s_1} & \frac{\partial f_1(s_0, s_1, s_2)}{\partial s_2} & \cdots & \frac{\partial f_1(s_0, s_1, s_2)}{\partial s_{n-1}} \\ \frac{\partial f_2(s_1, s_2, s_3)}{\partial s_0} & \frac{\partial f_2(s_1, s_2, s_3)}{\partial s_1} & \frac{\partial f_2(s_1, s_2, s_3)}{\partial s_2} & \cdots & \frac{\partial f_2(s_1, s_2, s_3)}{\partial s_{n-1}} \\ \vdots & \vdots & \vdots & \ddots & \vdots \\ \frac{\partial f_{n-1}(s_{n-1}, s_{n-2})}{\partial s_0} & \frac{\partial f_{n-1}(s_{n-1}, s_{n-2})}{\partial s_1} & \frac{\partial f_{n-1}(s_{n-1}, s_{n-2})}{\partial s_2} & \cdots & \frac{\partial f_{n-1}(s_{n-1}, s_{n-2})}{\partial s_{n-1}} \end{bmatrix} \tag{20}$$

The single-lap shear test is simulated by a displacement control that can be applied to either $x = n$ or $x = 0$ of the discretized bonded length (see Fig. 3). The main reason for choosing one of these two displacement control points lies in the need to capture the post-peak behaviour of the bonded interface. In other words, if the increment control s_0 (i.e. at $x = 0$) is adopted, then the snap-back phenomenon can be captured. Nevertheless, it should be kept in mind that the snap-back phenomenon can occur only when the bonded length is sufficiently long [69,70]. So, if the bonded length is short, i.e. shorter than the effective bond length, the full debonding process of the joint can be obtained by a monotonic slip control at $x = L$ (s_n). Thus, for the former case, Eq. (20) must be adjusted to the boundary condition of slip control increment at $x = 0$. Nevertheless, in both situations, the strains (ε_r) developed at the free end of the reinforcement is null and for this reason, the second boundary condition of the debonding problem is:

$$\frac{ds(x = 0)}{dx} = 0 \tag{21}$$

which leads to $s_1 = s_{-1}$ when Eq. (17) is used. Independently of the number of iterations needed to solve the problem stated in Eq. (19), the solution is found when:

$$\{s_i\}_{j+1} - \{s_i\}_j \approx 0 \tag{22}$$

2.6. Definition of the strains

After finding the slips developed throughout the bonded interface, the strains in the reinforcement and the substrate can be determined as well. To that end, the first derivative with respect to x of Eq. (4) is

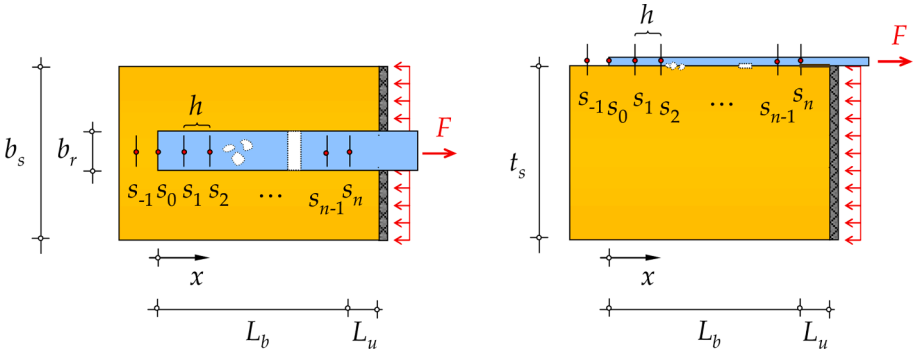

Fig. 3. Adopted discretization for the FRP-to-substrate bonded interface under the pull–push single-lap direct shear test.

considered, i.e.:

$$\frac{ds}{dx} = \frac{du_r}{dx} - \frac{du_s}{dx} \tag{23}$$

where du_r/dx and du_s/dx represent the strains developed in the reinforcement and substrate, respectively. Since the adherends have an elastic behaviour, Eq. (23) can be rewritten as:

$$\frac{ds}{dx} = \frac{\sigma_r}{E_r} - \frac{\sigma_s}{E_s} \tag{24}$$

By introducing Eq. (3) into Eq. (24) the strains developed in the reinforcement can be calculated according to:

$$\varepsilon_r = \frac{du_r}{dx} = \frac{1}{1+r}\frac{ds}{dx} \tag{25}$$

where r is the axial stiffness ratio of the bonded joint defined as follows:

$$r = \frac{E_r \cdot A_r}{E_s \cdot A_s} \tag{26}$$

Following an analogous procedure, the strains developed in the substrate can be determined as:

$$\varepsilon_s = \frac{du_s}{dx} = -\frac{1}{1+\frac{1}{r}}\frac{ds}{dx} \tag{27}$$

where ds/dx can be approximated by using Eq. (17).

3. SINGLE-LAP SHEAR TESTS

3.1. Experimental setup

The test setup was designed to test the CFRP-to-steel bonded joints free of any debonding defect. Fig. 4 shows the pull–push configuration test setup used to test the CFRP-to-steel single-lap bonded joints. To carry out the tests, the CFRP-to-steel joints (key number 7 in Fig. 4) were placed on the steel support indicated with no. 8 in Fig. 4. The CFRP laminate (no. 9 in Fig. 4) was placed inside the steel frame (no. 1 in Fig. 4) and went through the hydraulic jack (no. 5 in Fig. 4) and load cell (no. 2 in Fig. 4). It should be noted that the hydraulic jack is placed on a tubular support (no. 13 in Fig. 4) inside the steel frame. The loaded end of the CFRP laminate is mechanically anchored by steel wedges (no. 10 in Fig. 4). The steel substrate of the bonded joints is then constrained by a reaction steel plate (no. 6 in Fig. 4). The steel frame joint and the specimens are held by a metal profile (no. 12 in Fig. 4) against the lab strong floor (no.15 in Fig. 4) using four Dywidag rods (no. 3 in Fig. 4). Tests were performed in load control at an approximate rate of 150 N/min by using an hydraulic pump (no. 16 in Fig. 4). During the test, strains measured by strain gauges (no. 14 in Fig. 4) bonded onto the CFRP laminate and the load transmitted to the CFRP laminate were collected by a data logger (no. 18 in Fig. 4) and saved on a desktop computer (no. 17 in Fig. 4).

3.2. Mechanical properties of the materials and geometry of the specimens

The single-lap shear tests were performed on CFRP-to-steel bonded joints using a pull–push configuration. Two types of adhesives were considered: an epoxy resin S&P220 and Araldite® 2015. However, it should be noted that in this experimental work only the first resin was used. The S&P220 is a bi-component resin which consists of two different components, part A and part B, the resin and the hardener. The mechanical tests on 3 samples carried out in another work developed by the authors [71] concluded that the resin had an average elastic modulus of 0.79 GPa, an average tensile strength of 29.0 MPa, an average rupture strain of 3.65 %, and that it has an approximated linear elastic and brittle behaviour.

The unidirectional CFRP composite used in the experiments is 10 mm wide and 1.4 mm thick and its mechanical properties were obtained from five tensile tests carried out on a universal tensile machine with a load capacity of 50 kN. Within the direction of the carbon fibers, the tests showed a linear stress–strain relationship with a brittle rupture with an average elastic modulus of 159 GPa, an average strain rupture of 1.03 % and an average tensile strength of 1565 MPa. As a substrate, a hollow rectangular 3 mm-thick steel section was used in the single-lap

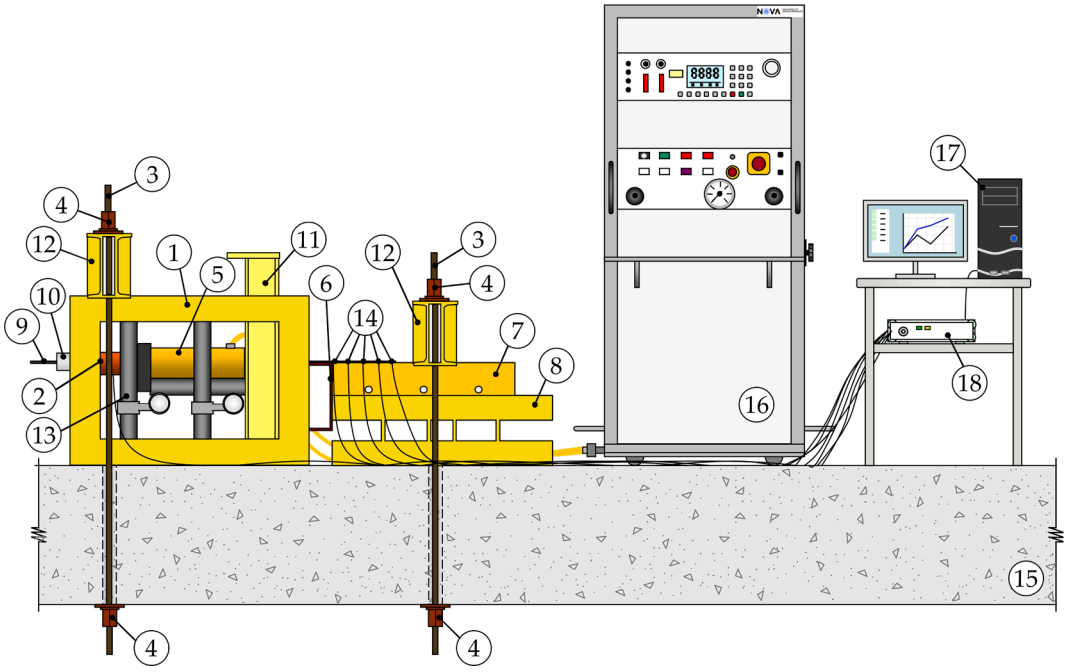

Fig. 4. Test setup. Key: 1 – Steel frame; 2 – Pressure cell; 3 – Dywidas steel rebar; 4 – Steel hex nut; 5 – hydraulic jack; 6 – Reaction steel profile; 7 – Steel substrate; 8 – Support steel profile; 9 –CFRP strip; 10 – Anchorage of the CFRP pulled end; 11 – Steel profile; 12 – Steel beam; 13 – Tubular frame; 14 – Strain gauges; 15 – Strong floor; 16 – Hydraulic pump; 17 – Desktop computer; 18 – Data logger.

shear tests. To preserve the geometry of the steel profiles, no experimental tests were carried out to determine the mechanical properties of the steel. Thus, an elastic modulus of the steel of 210 GPa was assumed. The steel unlikely would yield during the single-lap shear tests since it is much stronger than the CFRP-to-steel interface.

On the other hand, for the ductile adhesive, the work carried out by Wang et al. [67] is considered, in which structural Araldite® 2015 was used to bond an unidirectional CFRP strip to a steel plate. In this case [67], the CFRP was 50 mm wide and 1.4 mm thick. The mechanical properties of this CFRP composite were experimentally tested by Wang et al. [67], who determined the following average results in the carbon fiber direction: elastic modulus of 164 GPa, tensile strength of 2760 MPa, rupture strain of 1.68 %, and Poisson's ratio of 0.28. The adhesive used by Wang et al. [67] is strongly nonlinear and ductile and it has a high toughness. The tests of the resin flat coupons led to the following average mechanical properties: adhesive tensile strength of 15.1 MPa, elastic modulus of 1.75 GPa, rupture strain of 1.74 % and Poisson's ratio of 0.35 [67]. The steel had a tensile strength of 414 MPa, an elastic modulus of 198 GPa, yielding stress of 258 MPa, rupture strain of 29.4 %, and Poisson's ratio of 0.3, according to Wang et al. [67]. Furthermore, the CFRP composite was externally bonded onto a steel plate which was 20 mm thick, 138 mm wide and 380 mm long. The tests were monotonically carried out by pulling out the CFRP from the steel substrate mainly under Mode II conditions.

In these two cases, the single-lap shear tests reported here led to bond-slip relationships with similar maximum bond stresses. Thus, for this reason, the work developed by Wang et al. [67] was chosen to be replicated here by the proposed FDM, which allowed for making comparisons between both cases, i.e., with the CFRP-to-steel single-lap shear tests with a brittle and ductile adhesive, or, analogously, with a triangular and a trapezoidal bond-slip relationship, respectively. From all the experiments carried out by Wang et al. [67], the bond-slip relationship obtained from specimen A350-1.0–1 is considered. In this particular specimen, the maximum bond stress experimentally obtained under pure Mode II was $\tau_{bmax} = 13.70$ MPa, which is achieved when $s_1 = 0.053$ mm and begins to decay with a slip of $s_2 = 0.439$ mm, and it has a final slip of $s_f = 0.882$ mm [67]. This trapezoidal bond-slip relationship was reproduced by the nonlinear and single-function proposed in Eq. (13) and its accuracy in reproducing the experimental data can be seen in Fig. 2e.

3.3. Test results

The results obtained from the tests are briefly summarized in Table 1. For this study, four single-lap shear tests were considered among which, two different bonded lengths, a short and a long one of 50 mm and 200 mm were used, respectively. For each bonded length, the test was repeated two times with the same conditions. The strains developed in the CFRP laminate were measured by three and five strain gauges placed at equal distances of 25 mm and 50 mm on the specimens with $L_b = 50$ mm and $L_b = 200$ mm, respectively. It should be noted that during the test repetition of the specimen with $L_b = 200$ mm no data was collected due to an unexpected data logger error and therefore, only the data of the first test was considered (see Table 1).

The maximum loads obtained from the experiments are similar, which may indicate that the CFRP-to-steel joint may have a short effective bond length. The definition of the local bond behaviour of the CFRP-to-steel joints is carried out by calculating the bond stresses developed within the interface between the CFRP composite and the steel substrate. Hence, the following well-known expression, e.g. [72–75], is used:

$$\tau(x) = E_r t_r \cdot \frac{d\varepsilon_r}{dx} \tag{28}$$

which is obtained from the equilibrium of a finite section of the bonded length [76]. Its numerical solution can be approximated to:

$$\tau\left(x_{i+1/2}\right) = E_r t_r \cdot \frac{\varepsilon_{r,i+1} - \varepsilon_{r,i}}{x_{i+1} - x_i} \tag{29}$$

where the difference $x_{i+1} - x_i$ is the distance between two consecutive strain gauges; and $\varepsilon_{r,i+1}$ and $\varepsilon_{r,i}$ are the strains developed in the CFRP (i.e. the reinforcement) at the discretized points $i + 1$ and i, respectively.

To calculate the slips, Eq. (24) can be rearranged as follows:

$$ds = \left(\frac{\sigma_r}{E_r} - \frac{\sigma_s}{E_s}\right)dx = (\varepsilon_r - \varepsilon_s)dx \tag{30}$$

and then integrated with respect to x and solved by approximation as:

$$\begin{aligned} s(x_i) &= \int_{x_i}^{x_{i+1}} (\varepsilon_r - \varepsilon_s)dx + s(x_{i+1}) \\ &\approx \left(\frac{\varepsilon_{r,i+1} - \varepsilon_{s,i+1}}{2} - \frac{\varepsilon_{s,i} - \varepsilon_{r,i}}{2}\right)\cdot(x_{i+1} - x_i) + s(x_{i+1}) \end{aligned} \tag{31}$$

where $s(x_{i+1})$ is the slip at point x_{i+1}; $\varepsilon_{s,i+1}$ and $\varepsilon_{s,i}$ are the strains in the steel (i.e. the substrate) at points x_{i+1} and x_i, respectively; and $\varepsilon_{r,i+1}$ and $\varepsilon_{r,i+1}$ are the strains in the CFRP (or reinforcement) at points x_{i+1} and x_i, respectively. It should be noted also that if the stiffness of the substrate is much higher than that of the reinforcement, then Eq. (31) can be simplified and rewritten as:

$$s(x_i) = \int_{x_i}^{x_{i+1}} \varepsilon_r dx + s(x_{i+1}) \approx \frac{\varepsilon_{r,i+1} + \varepsilon_{r,i}}{2}\cdot(x_{i+1} - x_i) + s(x_{i+1}) \tag{32}$$

However, the bond stresses calculated in Eq. (29) correspond to the bond stresses at the centre of two consecutive strain gauges and the slips calculated in Eq. (31) or (32) correspond to the points where the strain gauges were mounted. Hence, to calculate the slips between consecutive points the average value was determined according to:

Table 1
Summary of the main results of the experimental tests.

Specimen	Test repetition	$\eta = A_d/A_b \times 100$ (%)	Maximum load, F_{max} (kN)	Maximum bond stress, τ_{bmax} (MPa)	Slip at maximum bond stress, s_1 (mm)	Final slip, s_f (mm)
CS50-W10-B_r-Ref-1	1	0	8.4	20.1	0.053	0.080
CS50-W10-B_r-Ref-2	2		7.6	25.4	0.049	0.110
CS200-W10-B_r-Ref-1	1	0	8.0	n/a	n/a	n/a
CS200-W10-B_r-Ref-2	2		7.2	15.5	0.085	0.550

n/a – data not available.

$$s\left(x_{i+1/2}\right) = \frac{s(x_{i+1}) + s(x_i)}{2} \tag{33}$$

Accordingly, the single-lap shear tests showed that the local bond behaviour had a triangular shape with maximum bond stress of τ_{bmax} = 13.27 MPa, a corresponding slip of s_1 = 0.096 mm, and a final slip of approximately s_f = 0.256 mm. Despite these results being based on a triangular bond-slip relationship, they were used to approximate the nonlinear single-function bond-slip relationship proposed in Eq. (13) to a triangular shape as shown in Fig. 2a.

From the work carried out by Wang et al. [67], the shortest and longest specimens were considered as well, i.e., specimens A70-1.0–1 and A350-1.0–1 were considered for comparison purposes. Specimens A70-1.0–1 and A350-1.0–1 have a bonded length of 70 mm and 350 mm, respectively. In both specimens, the same thickness of 1.0 mm was adopted for the adhesive. However, it should be noted that only the results obtained from specimen A350-1.0–1 were reported in detail and, therefore, the data to simulate specimen A70-1.0–1 were based on the local bond behaviour obtained from the former specimen. Considering all these factors, and covering a wider range of situations (including short and long bonded lengths), Table 2 identifies all specimens assumed in this work. Specimens in Table 2 were identified (ID) as: adherends (CFRP and Steel substrate), bonded length (L_b), Width of the CFRP composite (W), type of adhesive, i.e. brittle (B_r) or ductile (D_u), and the type of debonding defect, i.e. localized (L), dispersed (D) or reference (Ref) with no debonding defects, followed by the ratio between the multiple debonding defects and the total bonded area (herein denoted as η) as a percentage. Thus, as an example, the specimen denoted as CS200-W10-B_r-L50 means that the adherends are a CFRP (C) and steel (S) with a bonded length of 200 mm, where a 10 mm wide CFRP composite is bonded to the steel substrate with a brittle adhesive in which a localized debonding defect with η = 50 % is assumed.

3.4. Identification and characterization of the adopted multiple debonding defects

In this subsection, the characteristics of the multiple debonding defects considered in this work are described. Fig. 5 shows all the conditions for the four different bonded lengths and ratios between the multiple debonding defects and the total bonded area (η).

In addition, Fig. 6 shows the variation of parameter λ in its normalized form, i.e.:

$$\lambda_i^* = \frac{\lambda_i}{\lambda_0} \tag{34}$$

where parameters λ_i and λ_0 are, respectively, the values of parameter λ calculated according to Eq. (11) at point i and the corresponding reference value, i.e. considering full bonding of the FRP composite across its width. The results are plotted also considering the normalized bonded length of the joints defined as:

$$L_b^* = \frac{L_i}{L_b} \tag{35}$$

where L_i is the distance of point i from the FRP free end and L_b is the bonded length of the CFRP-to-steel joint. To allow for a fair comparison between specimens, the same distribution of the localized and dispersed debonding defects was kept the same independently of the bonded lengths of the CFRP-to-steel joints. As can be seen on the left-hand side of Figs. 5 and 6, the localized debonding defect was located at the centre of the CFRP-to-steel joints, whereas the dispersed debonding defect was randomly created so it could be obtained η = 25 %, 50 % and 75 % regardless of the bonded length of the joints (see Fig. 6).

4. Validation of the proposed FDM

4.1. Adopted strategy

To validate the proposed FDM, another numerical tool based on the Finite Element Method (FEM) was considered and all specimens identified in Table 2 were modelled. More details on the FEM used in this work are explained later. Bearing in mind that the present work aims to analyze the influence of multiple debonding defects on the FRP-to-substrate interface, two types of bonding defects were considered: (i) localized; and (ii) dispersed (or generalized). As mentioned before, the first case considers, for the sake of simplicity, one large debonded area that crosses the width of the FRP composite (see the left-hand side of Fig. 5), whereas the second case considers several small debonded areas that were randomly considered (see the right-hand side of Fig. 5). The corresponding single-lap shear tests were carried out with a CFRP externally bonded to a steel substrate and the results obtained in the experimental tests as well as those obtained by Wang et al. [67] were considered. Thus, for each bonded length, two different bond-slip relationships were considered and four ratios between the debonding defects and the total area (η) were assumed. It should be noted that the aim of assuming different bonded lengths was to capture the snap-back phenomenon identified in the literature, e.g. [77–79], in debonding problems and whose studies neglect the presence of multiple debonding defects. Hence, for the validation of the proposed FDM, a total of 112 different cases were modelled: 56 with the proposed FDM and the same number of specimens with the FEM.

4.2. Numerical modelling

Although other commercial software have been used in different studies [12,13,28,80–83] to simulate the contact between materials, the finite element commercial software ATENA package [84] was used in this work since it has proven its ability to estimate the bond behaviour between two adherends subjected either to pull-pull or pull–push tests, e.g. [57,68,85,86]. This software [84] has two versions, a 2D and a 3D version, but the 2D version was chosen since the number of unknowns and nonlinear equations to be solved by the Newton-Raphson method could be reduced significantly and both numerical simulations (FDM and FEM) could be compared. Another reason for choosing the 2D version of this software [84] is the computing time that is saved with no loss of precision in the simulations, as shown in the literature dealing with the debonding of CFRP composites from a substrate considered either rigid or deformable [85,86].

To simulate the contact between materials, ATENA software [84] uses a coupled cohesive model that is based on the Mohr-Coulomb criterion. Thus, when, for instance, peeling stresses develop within the contact between adherends, i.e., in the presence of Mode I, the stresses associated with Mode II (i.e. the shear stresses) are affected according to the Mohr-Coulomb criterion. Therefore, the friction angle (ϕ) adopted for the interface is of utmost importance for the correct simulation of the contact since it significantly controls the influence of Mode I on Mode II [57,68]. For instance, in a triangular bond-slip relationship, the friction angle value tends to increase the shear stresses in the presence of compression stresses (perpendicular to the bonded area). Also, under compressive stress, the interface develops a new F stage after the S stage of the predefined bond-slip relationship [57,68] that reflects the friction between adherends. However, if the interface is under tension, i.e., perpendicularly oriented in the opposite direction of the interface, only the bond stresses are affected by reducing their initial shear stress values at pure Mode II. It should be noted also that depending, for instance, on a misalignment of the load transmitted to the FRP composite, all these situations may affect any single point of the interface, which implies that at any point of the interface and under the presence of compression or tension stresses, different bond-slip relationships can be obtained throughout the bonded length. Therefore, the debonding phenomenon

Table 2
ID of the studied specimens subjected to the single-lap shear test simulations.

ID	Bonded length, L_b (mm)	Width of the CFRP composite, b_r (mm)	Adhesive type	Multiple debonding defects	$\eta = A_d/A_b \times 100$ (%)	Experimentally replicated
CS50-W10-B_r −Ref	50	10	Brittle	Reference	0	Yes
CS50-W10-B_r-L25				Localized	25	No
CS50-W10-B_r-L50					50	No
CS50-W-10-B_r-L75					75	No
CS50-W10-B_r-D25				Dispersed	25	No
CS50-W-10-B_r-D50					50	No
CS50-W10-B_r-D75					75	No
CS50-W10-D_u-Ref			Ductile	Reference	0	No
CS50-W10-D_u-L25				Localized	25	No
CS50-W10-D_u-L50					50	No
CS50-W10-D_u-L75					75	No
CS50-W10-D_u-D25				Dispersed	25	No
CS50-W10-D_u-D50					50	No
CS50-W10-D_u-D75					75	No
CS70-W50-B_r-Ref	70	50	Brittle	Reference	0	No
CS70-W50-B_r-L25				Localized	25	No
CS70-W50-B_r-L50					50	No
CS70-W50-B_r-L75					75	No
CS70-W50-B_r-D25				Dispersed	25	No
CS70-W50-B_r-D50					50	No
CS70-W50-B_r-D75					75	No
CS70-W50-D_u-Ref			Ductile	Reference	0	Yes[(1)]
CS70-W50-D_u-L25					25	No
CS70-W50-D_u-L50					50	No
CS70-W50-D_u-L75					75	No
CS70-W50-D_u-D25					25	No
CS70-W50-D_u-D50					50	No
CS70-W50-D_u-D75					75	No
CS200-W10-B_r-Ref	200	10	Brittle	Reference	0	Yes
CS200-W10-B_r-L25				Localized	25	No
CS200-W10-B_r-L50					50	No
CS200-W10-B_r-L75					75	No
CS200-W10-B_r-D25				Dispersed	25	No
CS200-W10-B_r-D50					50	No
CS200-W10-B_r-D75					75	No
CS200-W10-D_u-Ref			Ductile	Reference	0	No
CS200-W10-D_u-L25				Localized	25	No
CS200-W10-D_u-L50					50	No
CS200-W10-D_u-L75					75	No
CS200-W10-D_u-D25				Dispersed	25	No

(*continued on next page*)

Table 2 (*continued*)

ID	Bonded length, L_b (mm)	Width of the CFRP composite, b_r (mm)	Adhesive type	Multiple debonding defects	$\eta = A_d/A_b \times 100$ (%)	Experimentally replicated
CS200-W10-D_u-D50					50	No
CS200-W10-D_u-D75					75	No
CS350-W50-B_r-Ref	350	50	Brittle	Reference	0	No
CS350-W50-B_r-L25				Localized	25	No
CS350-W50-B_r-L50					50	No
CS350-W50-B_r-L75					75	No
CS350-W50-B_r-D25				Dispersed	25	No
CS350-W50-B_r-D50					50	No
CS350-W50-B_r-D75					75	No
CS350-W50-D_u-Ref			Ductile	Reference	0	Yes[(2)]
CS350-W50-D_u-L25				Localized	25	No
CS350-W50-D_u-L50					50	No
CS350-W50-D_u-L75					75	No
CS350-W50-D_u-D25				Dispersed	25	No
CS350-W50-D_u-D50					50	No
CS350-W50-D_u-D75					75	No

[(1)] Denoted as A70-1.0–1 by Wang et al. [67] but no load-slip curve or bond-slip relationship was reported;
[(2)] Denoted as A350-1.0–1 by Wang et al. [67].

between adherends can be simulated as close as possible to reality.

Fig. 7 shows two different numerical models typically considered in this work. Thus, as an example, Fig. 7a shows the numerical model of the specimen with a localized debonding defect area of $\eta = 25$ % and a bonded length of 200 mm (i.e. CS200-W10-B_r-L25 or CS200-W10-D_u-L25), whilst Fig. 7b shows model A350-1.0–1 tested by Wang et al. [67] and numerically simulated by Wang et al. [87], which has a bonded length of 350 mm (i.e. specimens CS350-W50-B_r-L25 or CS350-W50-D_u-L25). The loads transmitted to the CFRP-to-steel joints *versus* the slip at the loaded end (or for simplicity load-slip curves) are all analyzed, allowing to highlight differences obtained from specimens with multiple debonding defects and their corresponding results obtained from the reference models.

Since the Integral Absolute Error (IAE) is a parameter sensitive to the deviation of a theoretical result from an experimental data, at the same time, it is often used for model assessment, e.g. [88–90], this parameter was chosen to assess the accuracy of the load-slip curves obtained by the proposed FDM when compared with the results obtained by the FEM. It was calculated according to the following expression:

$$IAE = \sum_{s=1}^{n} \frac{\left| f^{FDM} - f^{FEM} \right|}{\sum_{s=1}^{n} f^{FEM}} \tag{36}$$

where f^{FDM} and f^{FEM} correspond to the loads obtained from the proposed FDM and those calculated from the FEM at the same slip at the CFRP loaded end, respectively, for the same interfacial slip s; and n corresponds to the number of measurements carried out during the simulations.

The models simulated in ATENA software [84] were all discretized through a mesh with 0.4 to 0.5 mm quadrilateral finite elements (with smooth element shapes), near the contact between materials as shown in Fig. 7. Moreover, to avoid an excessive increase in the number of finite elements, the specimens with a bonded length of 350 mm had larger quadrilateral finite elements (5 mm) at the bottom of the model (see detail in Fig. 7b). Due to the different heights of the steel substrate and bonded lengths of the CFRP-to-steel joints, the number of finite elements used in each one was different. So, in the case of the model with the fewest finite elements, i.e., with $L_b = 50$ mm, a total of 1306 finite elements were used, whereas the models with the highest number of finite elements, i.e., specimens with $L_b = 350$ mm, had a total of 9518 finite elements.

The loads applied to the CFRP composite were simulated by imposing a monotonic displacement with a rate of 0.002 mm per step at the right hand side of the model as can be seen in Fig. 7. At the reaction steel plate, there was another monitoring point whose results were used for comparison with the loads transmitted to the CFRP material (i.e. redundant data to control the evolution and feasibility of the numerical simulations). To avoid the rotation of the specimen a horizontal roller support was placed at the left-hand side of the models (see Fig. 7). To ensure complete debonding of each simulated specimen, the number of steps considered in each model varied so failure could be achieved.

Eight single-lap shear tests with no initial debonding defects were simulated first with ATENA software [84] and the results were used as reference values. The main results obtained for each specimen modelled in this work are summarized in Table 3.

4.3. Bond behaviour of CFRP-to-steel joints with no debonding defects

All load-slip curves obtained for the reference specimens, i.e., free of any debonding defects, are shown in Fig. 8. However, it should be noted that only the tested specimens with a brittle adhesive and bonded lengths of 50 mm and 200 mm (see Fig. 8a) are shown, as well as the specimen with a ductile adhesive and bonded length of 350 mm tested by Wang et al. [67] (specimen A350-1.0–1) (see Fig. 8d).

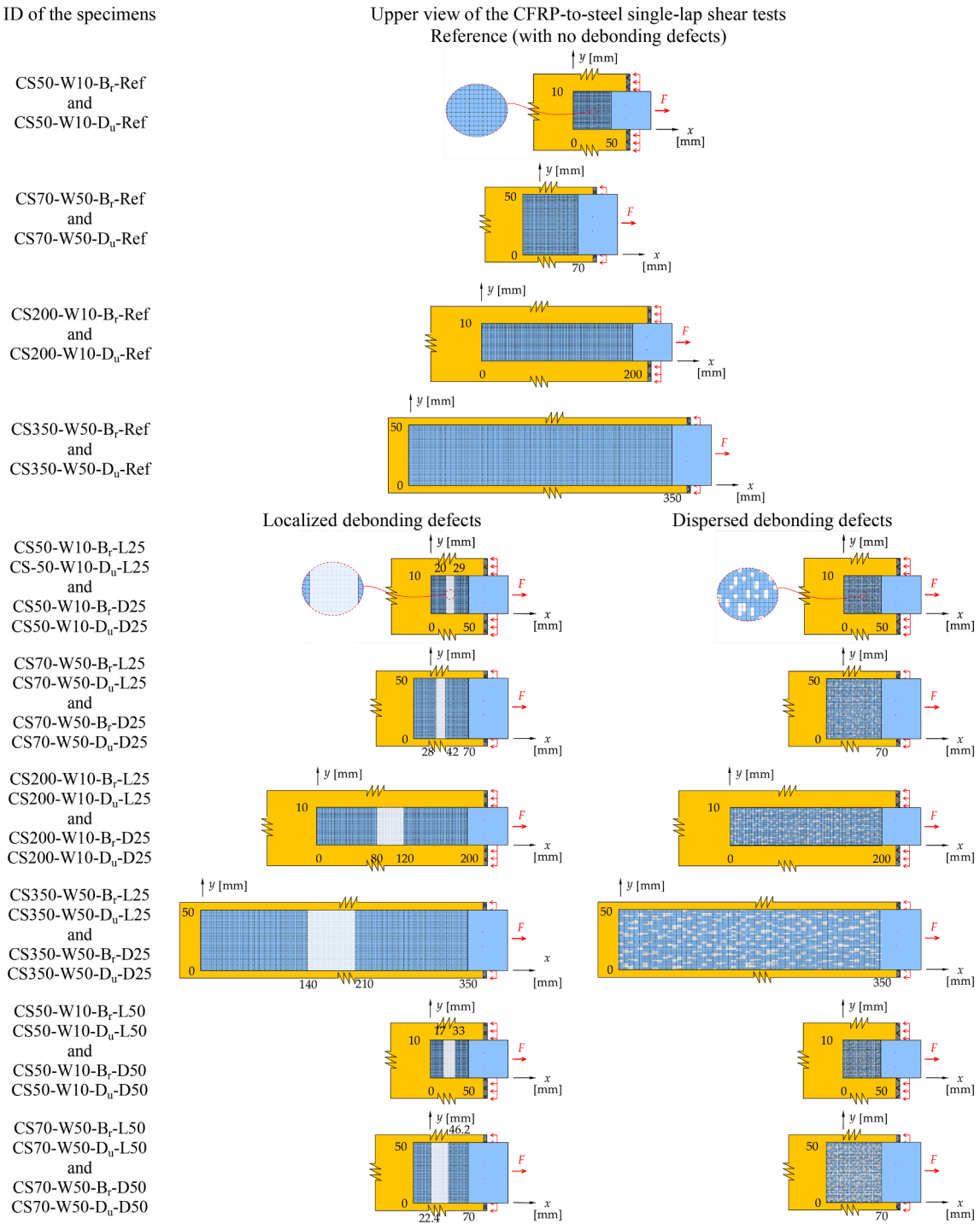

Fig. 5. Characterization of the multiple debonding defects of all specimens considered in this work.

The experimental data show a higher initial stiffness when compared with the proposed FDM and FEM and only the experimental data obtained from the specimen CS200-W10-B_r-Ref-2 (see Table 1) had a maximum load lower than that obtained from both numerical methods. The maximum load predicted by the proposed FDM and by the FEM for specimen CS200-W10-B_r-Ref reached 9.19 kN and 8.82 kN, respectively, which are approximately 27.6 % and 22.5 % higher than the experimentally determined values (7.20 kN as shown in Table 3). The maximum loads experimentally reached by specimens CS50-W10-B_r-Ref-1 and CS50-W10-B_r-Ref-2 had an average value approximately 22.8 % higher (8.00 kN as shown in Table 3) than that obtained by the FDM or FEM (6.19 kN and 6.17 kN in specimen CS50-W10-Br-Ref shown in Table 3). Also, Wang et al. [67] reported that specimen A350-1.0–1 reached a maximum load value of 108.5 kN, which is approximated 11.4 % higher than that obtained by both numerical simulations, which reached approximately 97.4 kN.

Nevertheless, the numerical simulations carried out by the proposed FDM are consistent with those obtained from the FEM and coincident with the load-slip curves obtained in other studies available in the literature, e.g. [69,77,78]. For instance, both models have predicted very well all the reference specimens in all branches of the load-slip curves. For instance, in all specimens, the ascending branches are quite similar. Unlike the specimen with a brittle adhesive with $L_b = 200$ m, the specimen with $L_b = 50$ mm does not show a plateau at maximum

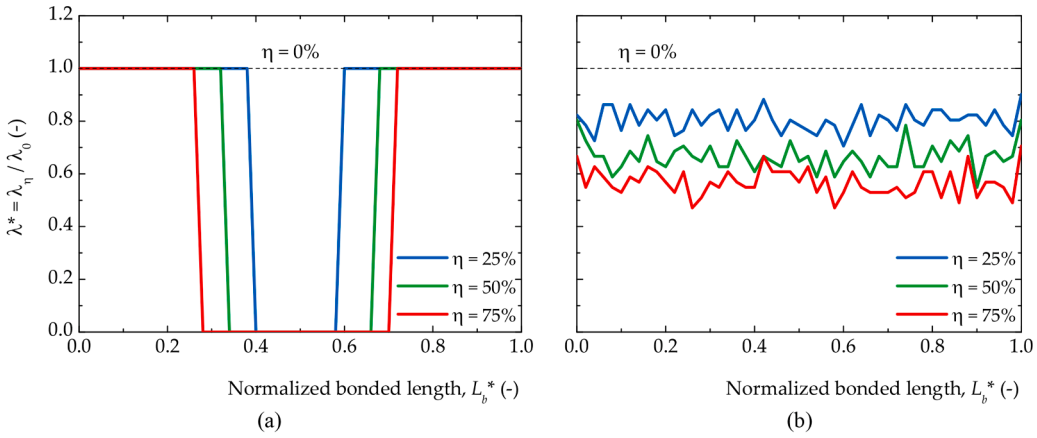

Fig. 6. Variation of the normalized parameter λ with the normalized bonded length of the joints (L_b*) with: (a) a localized debonding defect; and (b) a dispersed debonding defect.

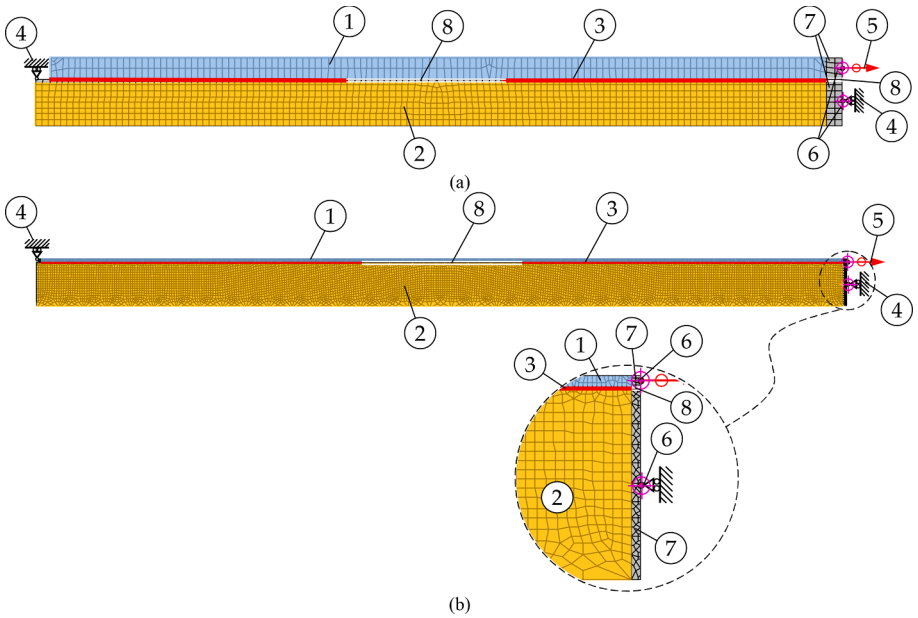

Fig. 7. Examples of the finite element meshes of the CFRP-to-steel single-lap shear test of specimens CS50-W10-B_r-L25 (or D_u) and CS350-W50-B_r-L25 (or D_u) with a localized debonding defect of η = 25 % with: (a) L_b = 50 mm; and (b) L_b = 350 mm.

load and a peak load is reached instead before the load begins to decrease smoothly until the complete debonding between adherends.

In the case of the specimens with a ductile adhesive, a plateau can be observed in all specimens independently of the bonded length. In these cases, the plateau at maximum load shown in the specimens with L_b = 50 mm and L_b = 70 mm develops due to the C stage of the bond-slip relationship (see Fig. 2e). However, as the bonded length increases up to 200 mm or 350 mm, the maximum load increases and the post-peak behaviour predicted by the FDM shows the snap-back phenomenon, which means that this bonded length is sufficiently long. Note that the specimen with L_b = 350 mm has a CFRP five times the width of the other specimen with L_b = 200 mm and since the maximum load is the only parameter that is directly proportional to the width of the FRP composite [1,39,42,53,91], this means that the maximum load would also increase of approximately five times. So, the maximum load of 18.78 kN was reached in specimen CS200-W10-D_u-Ref, whereas in specimen A350-1.0–1 a maximum load of 97.44 kN was determined, which is approximately 5.2 times the load of the specimen with L_b = 200 mm and width 10 mm.

Except for specimen CS50-W10-Ref-B_r in which the corresponding IAE value reached approximately 12.0 %, all the other IAE values never exceeded 10 %. Therefore, these results show that the proposed FDM led to accurate results. Furthermore, in the specimens with a ductile adhesive (see Fig. 8c and 8d), the maximum IAE values are all lower than 3.5 %. It should also be noted that since the snap-back behaviour observed in the specimens with the longest bonded lengths cannot be predicted by the FEM by using the Newton-Raphson method, the IAE values were calculated up to the reverse of the slips was reached in the load-slip curves.

4.4. Bond behaviour of CFRP-to-steel joints with a brittle adhesive

The load-slip curves obtained for the different CFRP-to-steel joints with a brittle adhesive are shown in Fig. 9. Based on these results, it is possible to observe that when the bonded length is short (e.g., 50 mm and 70 mm), the shape of the corresponding reference load-slip curve

Table 3
Summary of the main results and comparisons between the proposed FDM with ATENA software [84].

Specimen	Multiple debonding defect type	$\eta = A_d/A_b \times 100$ (%)	Maximum load, F_{max} (kN)			Load degradation (−)
			Proposed FDM	ATENA [84]	Deviation (%)	
CS50-W10-B_r-Ref	Reference	0	6.19 (8.00)*	6.17	0.32	1
CS50-W10-D_u-Ref			6.73	6.80	−1.03	1
CS50-W10-B_r-L25	Localized	25	5.03	5.15	−2.33	0,813
CS50-W10-D_u-L25			5.40	5.58	−3.23	0,802
CS50-W10-B_r-L50		50	4.19	4.32	−3.01	0,677
CS-50-W10-D_u-L50			4.47	4.63	−3.46	0,664
CS50-W10-B_r-L75		75	3.60	3.72	−3.23	0,582
CS50-W10-D_u-L75			3.80	3.95	−3.80	0,565
CS50-W10-B_r-D25	Disperse	25	5.07	5.05	0.40	0,819
CS50-W10-D_u-D25			5.41	5.44	−0.55	0,804
CS50-W10-B_r-D50		50	4.25	4.29	−0.93	0,687
CS50-W10-D_u-D50			4.48	4.56	−1.75	0,666
CS50-W10-B_r-D75		75	3.65	3.66	−0.27	0,590
CS50-W10-D_u-D75			3.82	3.86	−1.04	0,568
CS70-W50-B_r-Ref	Reference	0	39.31	38.45	2.24	1
CS70-W50-D_u-Ref			47.10	47.61	−1.07	1
CS70-W50-B_r-L25	Localized	25	32.45	32.31	0.43	0,826
CS70-W50-D_u-D25			37.78	38.09	−0.81	0,802
CS70-W50-B_r-L50		50	27.57	27.64	−0.25	0,701
CS70-W50-D_u-D50			31.25	31.62	−1.17	0,664
CS70-W50-B_r-L75		75	23.62	23.64	−0.09	0,601
CS70-W50-D_u-L75			26.59	26.95	−1.34	0,565
CS70-W50-B_r-L25	Disperse	25	33.00	32.31	2.14	0,840
CS70-W50-D_u-L25			37.87	38.19	−0.84	0,804
CS70-W50-B_r-L50		50	28.13	27.79	1.22	0,716
CS70-W50-D_u-L50			31.35	31.62	−0.85	0,666
CS70-W50-B_r-L75		75	24.48	24.22	1.07	0,623
CS70-W50-D_u-L75			26.75	26.95	−0.74	0,568
CS200-W10-B_r-Ref	Reference	0	9.19 (7.60)*	8.82	4.20	1
CS200-W10-D_u-Ref			18.78	18.67	0.59	1
CS200-W10-B_r-L25	Localized	25	8.72	8.42	3.56	0,949
CS200-W10-D_u-L25			16.43	16.27	0.98	0,875
CS200-W10-B_r-L50		50	8.29	8.00	3.63	0,902
CS200-W10-D_u-L50			14.74	14.56	1.24	0,785
CS200-W10-B_r-L75		75	7.88	7.61	3.55	0,857
CS200-W10-D_u-L75			13.43	13.28	1.13	0,715
CS200-W10-B_r-D25	Disperse	25	8.20	7.87	4.19	0,892
CS200-W10-D_u-D25			16.74	16.65	0.54	0,891
CS200-W10-B_r-D50		50	7.41	7.15	3.64	0,806
CS200-W10-D_u-D50			15.06	15.12	−0.40	0,802
CS200-W10-B_r-D75		75	6.84	6.59	3.79	0,744
CS200-W10-D_u-D75			13.65	13.69	−0.29	0,727
CS350-W50-B_r-Ref	Reference	0	47.82	45.88	4.22	1
CS350-W50-D_u-Ref			97.44 (108.5)*	97.37	0.07	1
CS350-W50-B_r-L25	Localized	25	47.49	45.57	4.21	0,993
CS350-W50-D_u-L25			94.45	93.36	1.17	0,969
CS350-W50-B_r-L50		50	47.33	45.33	4.41	0,990
CS350-W50-D_u-L50			92.22	90.79	1.58	0,950
CS350-W50-B_r-L75		75	46.90	45.00	4.22	0,981
CS350-W50-D_u-L75			87.22	85.35	2.19	0,895
CS350-W50-B_r −D25	Disperse	25	43.08	41.30	4.31	0,901
CS350-W50-D_u-D25			87.77	87.20	0.65	0,901
CS350-W50-B_r-D50		50	39.03	37.50	4.08	0,816
CS350-W50-D_u-D50			79.58	79.07	0.64	0,817
CS350-W50-B_r-D75		75	36.54	35.13	4.01	0,764
CS350-W50-D_u-D75			73.64	73.66	−0.03	0,756

* Experimental average value between parentheses.

does not change with multiple debonding defects, whether localized or dispersed. However, looking at specimens with the longest bonded lengths, the shape of the load-slip curves is different depending of the debonding defect type considered. In these specimens, the loads increase first with an approximately linear trend with the slips at the loaded end. Before reaching maximum load, a nonlinear behaviour is observed due to the development of the S stage close to the CFRP-loaded end. For the reference specimens, a plateau at maximum load can be observed in Fig. 9e and 9 g. The post-peak behaviour is captured by the proposed FDM since the slip control adopted for the debonding process was located at the CFRP-free end and, therefore, the well-known snap-back phenomenon could be captured. It should also be kept in mind that since the slip control carried out in the FEM is located at the CFRP loaded end, the post-peak behaviour of these models cannot be captured when the Newton-Raphson method is used and, therefore, no comparisons between the proposed FDM and the FEM can be made there.

Moreover, the results obtained from these specimens with a localized debonding defect show two peak loads. After the first peak load, a decrease of the load is observed and then the load begins to increase again. Such behaviour can be explained by the fully bonded length localized near the CFRP-free end contributing to the second load increase. Although not observed in all specimens, it can be asseverated that if the localized debonding defect was placed closer to the CFRP-loaded end, a snap-through phenomenon would be possible to observe

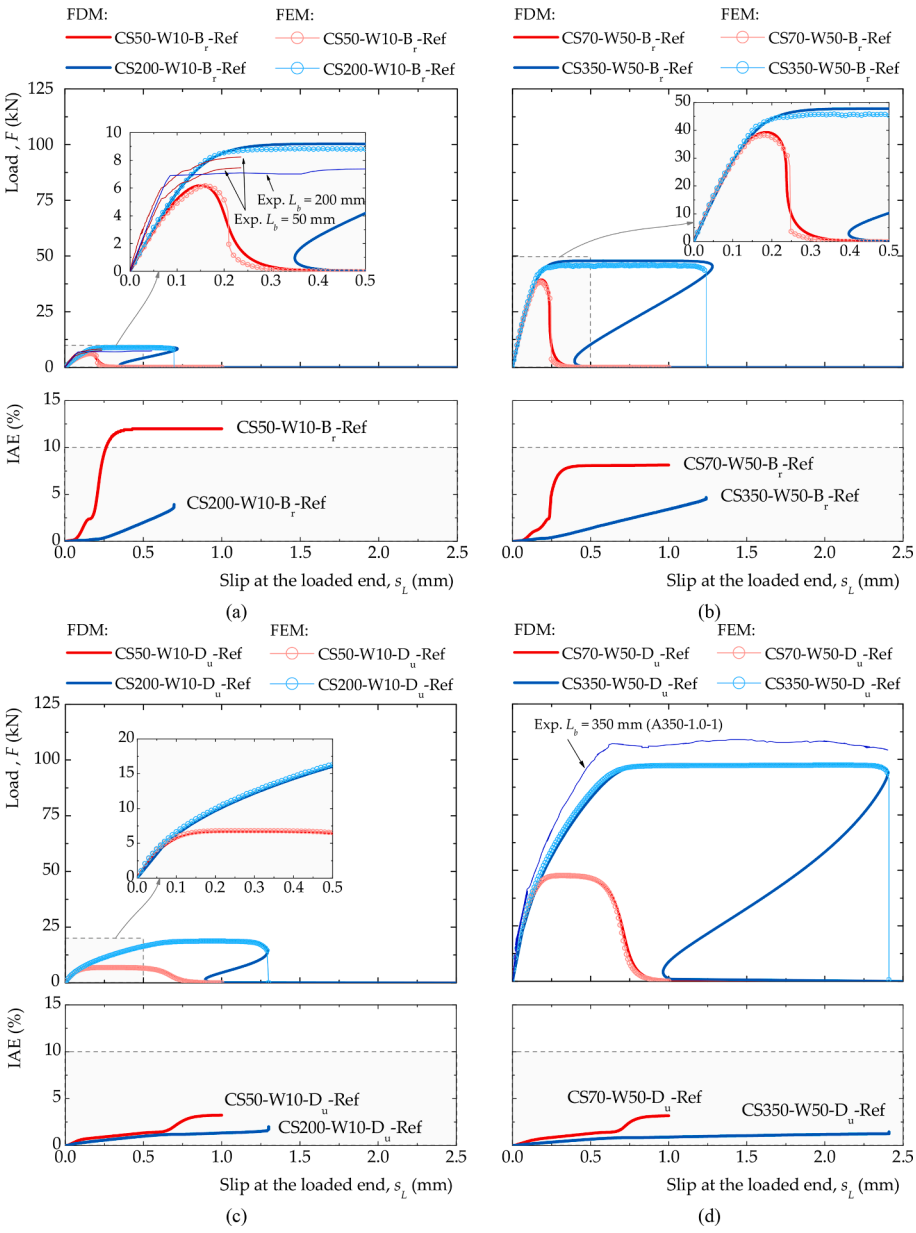

Fig. 8. Comparison between the load vs. slip at the loaded end curves obtained from the proposed FDM and from the FEM based on the: (a) present experimental work (with a brittle adhesive); (b) work carried out by Wang et al. [67] with the brittle adhesive used in the present work; (c) present work with the ductile adhesive obtained by Wang et al. [67]; (d) work carried out by Wang et al. [67].

more easily. Nevertheless, such a snap-through phenomenon can be observed, e.g., in specimen CS350-W50-Br-L25 (see Fig. 9g). In addition, the load-slip curve, in such cases, would also be characterized by a snap-back phenomenon, independently of the bonded length or debonding defect type.

If the multiple debonding defect is dispersed, the shape of the load-slip curve only slightly changes with the ratio between the debonding defects and the bonding area (η). Thus, in the presence of a dispersed debonding defect, the load capacity of the specimens decreases but the shape of the load-slip curve shows almost no change from the reference results. However, the extend of the plateau at maximum load tends to decrease with the increase of η, which means that the ductility of the joint also decreases.

The IAE values herein determined never reached 15 % and for the specimens with the longer bonded lengths, the value never exceeded 5 %, which shows how close the proposed FDM is to the data obtained from the FEM. The higher IAE values are associated with the specimens with the lowest load capacities, i.e. the specimens with the shortest bonded lengths. In general, the IAE values also tended to increase slightly with the increase of η. The results obtained show taht the proposed FDM is validated for the CFRP-to-steel joints with a brittle adhesive, independently of the multiple debonding defects of the joint, i.e. whether the pattern is localized or dispersed.

4.5. *Bond behaviour of CFRP-to-steel joints with a ductile adhesive*

Considering a ductile adhesive with the local bond behaviour represented in Fig. 2e, Fig. 10 shows the load-slip curves obtained from all specimens, either from the proposed FDM or from the FEM. The results are, once again, compared with the reference specimens with η = 0 %. Similar to the joints with a brittle adhesive, the shape of the load-slip curves of the CFRP-to-steel joints with the shortest bonded lengths (e.g., 50 mm and 70 mm), did not change with the localized or dispersed debonding defect type. Moreover, regarding the two debonding defect

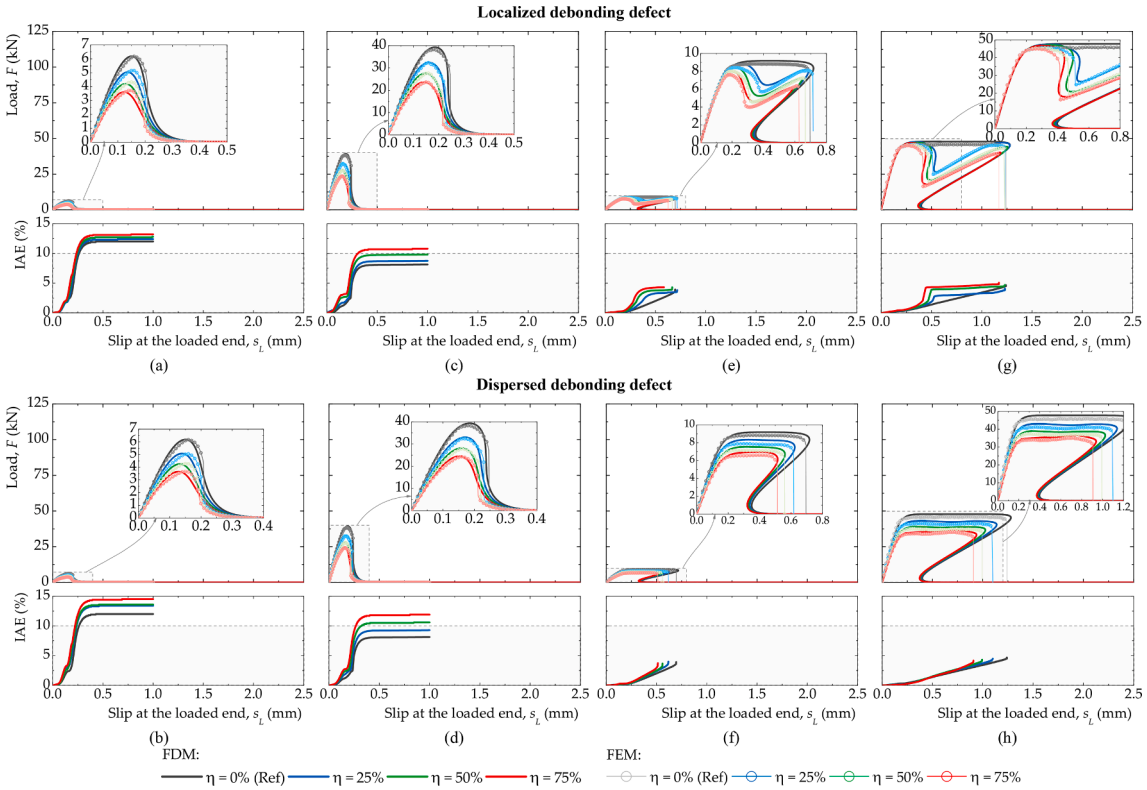

Fig. 9. Precision of the proposed FDM in the determination of the load vs. slip at the loaded end curves of the tests with a CFRP composite with a brittle adhesive and: (a)-(b) $L_b = 50$ mm; (c)-(d) $L_b = 70$ mm; (e)-(f) $L_b = 200$ mm; and (g)-(h) $L_b = 350$ mm.

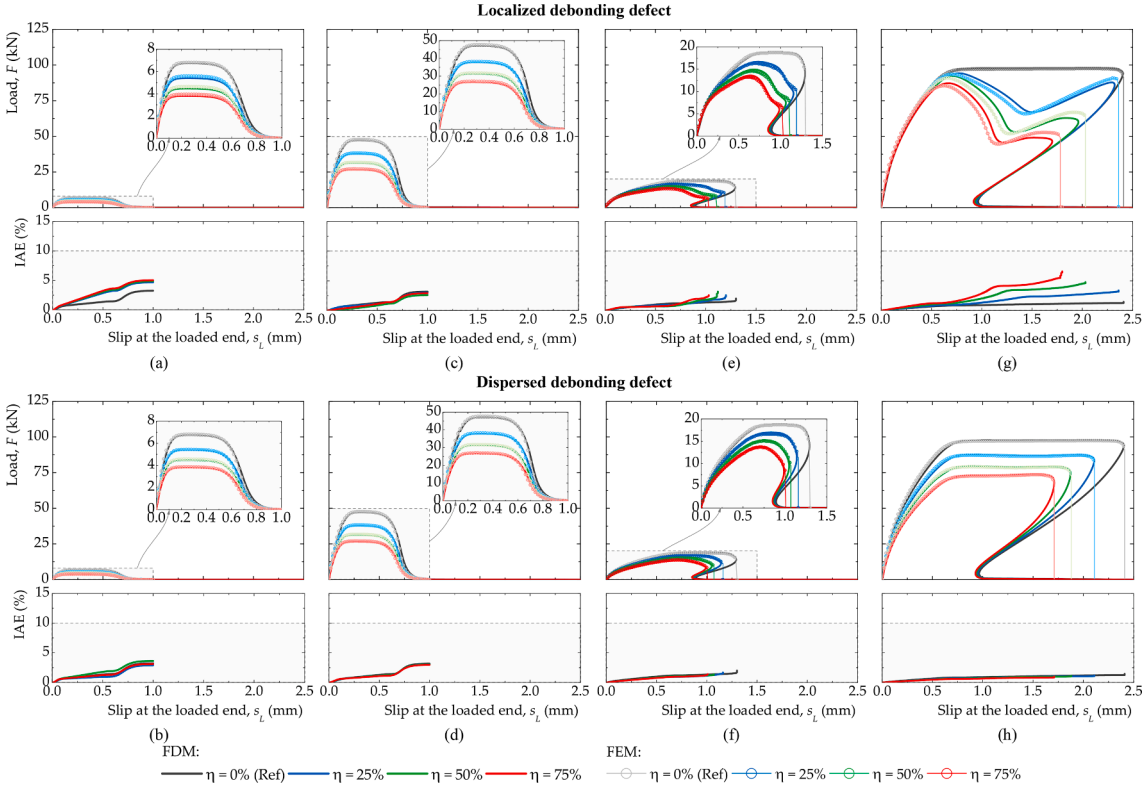

Fig. 10. Precision of the proposed FDM in the determination of the load vs. slip at the loaded end curves of the tests with a CFRP composite with a ductile adhesive and: (a)-(b) $L_b = 50$ mm; (c)-(d) $L_b = 70$ mm; (e)-(f) $L_b = 200$ mm; and (g)-(h) $L_b = 350$ mm.

types, the degradation of the load capacities did not change significantly with the increase of η.

However, analyzing at the load-slip curves obtained from the joints with the longest bonded lengths (200 mm and 350 mm), some differences can be observed. For instance, in the case of L_b = 200 mm, the specimens with localized debonding defect show a tendency of the joint to reach another, although quite short, plateau stage after its post-peak behaviour. This can be explained by the transition of the loads from the first bonded area to the second one. However, since the bond-slip relationship of the ductile adhesive can accommodate higher slips, a higher effective bond length of these joints is expected [42]. Thus, after the specimens have reached their load peak, no increase in the loads is observed in these joints (see Fig. 10e and 10f). Unlike the localized debonding defect case, the loads transmitted to the CFRP composite in the specimens with a dispersed debonding defect decrease with no tendency to increase again. Nevertheless, the specimens with L_b = 350 mm and with a localized debonding defect had a sufficient bonded length to show another load increase after the load capacity of the joints was reached (see Fig. 10g). The specimens with a dispersed debonding defect show a similar plateau at maximum load to that which is observed in the reference specimen and only a slight influence is noted with the increase of η (see Fig. 10*h*). However, a general tendency of joints with a debonding defect to decrease their ductility can be observed.

Unlike some results obtained from adopting a brittle adhesive in joints with the shortest bonded lengths, where the IAE values ranged between 10 % and 15 %, the IAE values obtained by using a ductile adhesive barely exceeded 5 %. These differences might be explained by the definition of both bond-slip relationships in the FEM whose data was based on small and linear intervals that could be sufficient to numerically describe the local adherence of these joints. Nevertheless, in both cases of brittle and ductile adhesive, about 50 intervals of 0.01 mm each were assumed. Thus, it would be expected that the increase in the number of intervals would decrease the IAE values obtained for the specimens with the shortest bonded lengths with a brittle adhesive, since the nonlinearities of the corresponding bond-slip relationship may be even more refined. Yet, and based on the present results, the validation of the proposed FDM can be considered as having been achieved successfully.

4.6. Degradation of the load capacity of the joints

The influence of the debonding defects on the load capacity of the CFRP-to-steel bonded joints is analyzed in this section. The degradation of the loads (D_L) with parameter η is shown in Fig. 11, in which their values were determined as:

$$D_L = \frac{F_{\max,\eta} - F_{\max,0}}{F_{\max,0}} \times 100\% \tag{37}$$

where $F_{\max,\eta}$ and $F_{\max,0}$ are, respectively, the maximum load reached by the specimens with a debonding defect whose values are within the interval of 0 % < η < 100 % and the maximum load reached by the corresponding reference specimens, i.e. with no debonding defects (η = 0 %).

The results show that the CFRP-to-steel joints with the shortest bonded lengths were marginally influenced either by the debonding defect type or by the adhesive type (see Fig. 11a and 11b). However, a

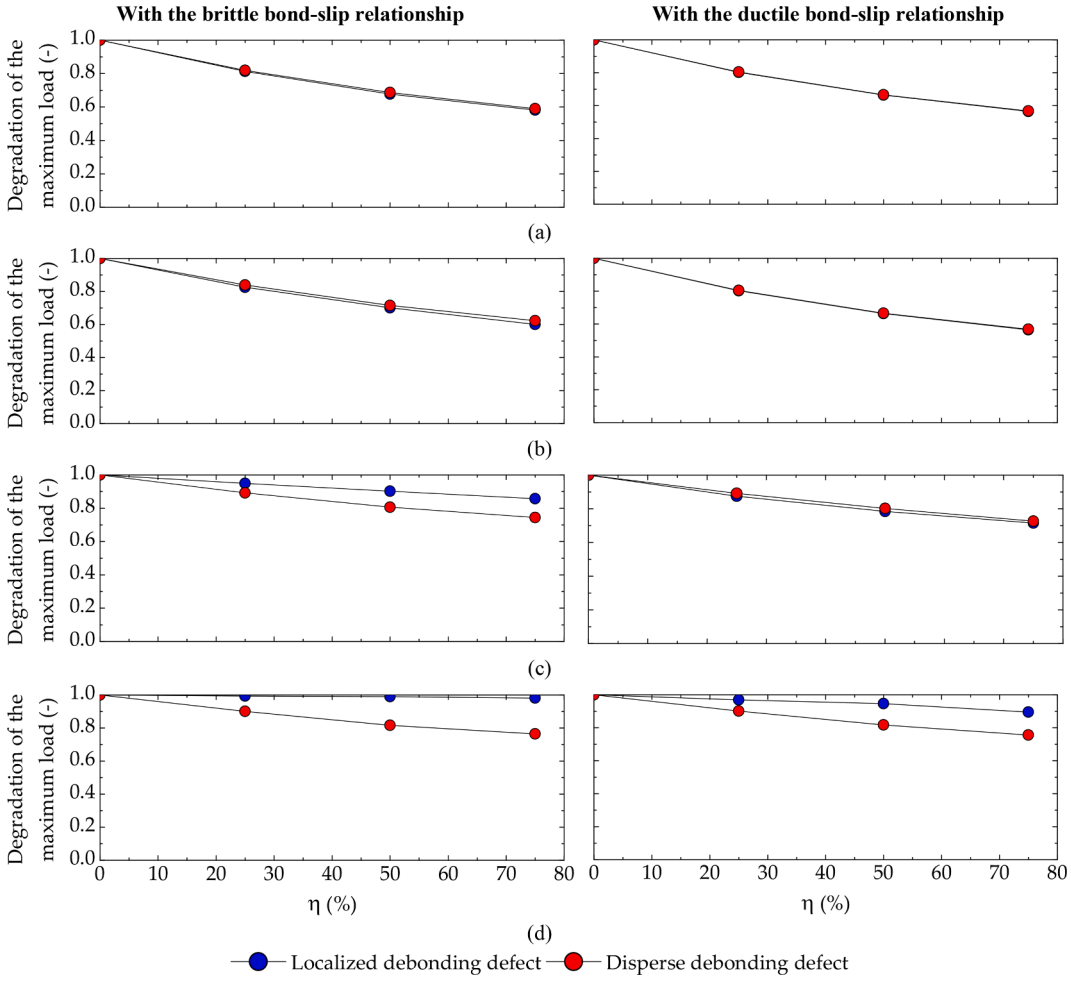

Fig. 11. Influence of the adhesive type on the load capacity of the CFRP-to-steel joints with: (a) L_b = 50 mm; (b) L_b = 70 mm; (c) L_b = 200 mm; and (d) L_b = 350 mm.

maximum load degradation of approximately 40 % was determined in all cases with η = 75 %. As longer bonded lengths are considered, the brittle adhesive begins to show a different load degradation path between the localized and the dispersed debonding defects (see Fig. 11c). In this case, the multiple dispersed debonding defects lead to the highest load degradations for any values of η herein considered.

Contrary to this, the localized debonding defect leads to a lower load degradation of the specimens with the longest bonded lengths, which means that this debonding defect has a low influence on the load capacity of the joint (see Fig. 11d). For instance, in the case of specimen CS350-W50-B_r-L75, a degradation of approximately 2.0 % was measured, whilst specimen CS350-W50-B_r-D75 had a load degradation of approximately 23.6 % (see left-hand side of Fig. 11d). From the analogous specimens with a ductile adhesive (see right-hand side of Fig. 11d), load degradations of approximately 10.5 % and 24.4 % were calculated for the specimens with the localized and dispersed debonding defects, respectively.

5. Comparisons with other work available in the literature [87]

The results of the tests carried out by Wang et al. [87] are compared with the results obtained from the proposed FDM in this section. It should be noted that no other studies were found in the literature that could cover the influence of multiple debonding defects within the CFRP-to-steel interface, and for this reason no other studies were considered in this work.

In the work developed by Wang et al. [87], a strip-model numerical strategy based on the explicit 4th-order Runge-Kutta technique was proposed and a trapezoidal bond-slip relationship was used to model the local bond behaviour between the CFRP composite and the steel substrate. The mechanical properties of the CFRP composite and the steel plate were based on another work carried out by Wang et al. [67]. Therefore, the definition of the trapezoidal bond-slip relationship is the same as the one mentioned earlier at the end of Subsection 3.1 and fitted by a single-function bond-slip relationship as shown in Fig. 2e. Similarly, the geometry and dimensions of the specimens are the same as those briefly described in Subsection 3.1. The models herein reproduced were originally designated as A180-AD and A200-AD [67], which means that a bonded length of, respectively, 180 mm and 200 mm was considered. However, the geometry of the debonding defects in the two specimens is different, as shown in Fig. 12. Overall, both their debonding defects are described as localized. Specimen A180-AD has one localized debonding defect at the centre of the joint with a corresponding η value of approximately 28 %, whilst specimen A200-AD has two localized debonding defects with η ≈ 37 %. To facilitate the identification and evaluation of how damaged the interface between the adherends is, Fig. 13 shows the variation of λ_i^* with L_b^* according to Eq. (34) and Eq. (35), respectively.

Fig. 14 shows the precision of the proposed FDM on the prediction of the specimens by Wang et al. [87]. The maximum load of specimen A180-AD predicted by the proposed FDM was 82.18 kN, whilst Wang et al. [87] reported a value of 83.02 kN that corresponds to a deviation of approximately −1.0 %. On the other hand, the proposed FDM predicted a maximum load of 79.52 kN for specimen A200-AD, whilst Wang et al. [86] reported a value of 85.09 kN that represents a deviation of approximately −6.5 %.

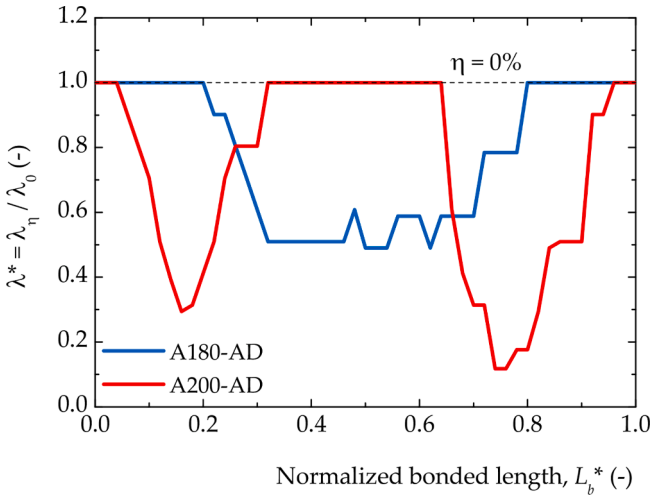

Fig. 13. Variation of the normalized parameter λ with the normalized bonded length of the specimens tested by Wang et al. [87].

Furthermore, the proposed FDM was shown to be able to follow the full data provided by Wang et al. [87], which means that all stages (i.e. Elastic, Constant, Softening, and Debonding) defined by the bond-slip relationship as well as the influence of the multiple debonding defects were well predicted. In both specimens, the loads show an initial increase with a stiffness that tends to decrease due to the influence of the localized debonding defects. Afterwards, an approximately linear increase of the loads can be observed, which means that the E stage is still predominant within the CFRP-to-steel interface. However, before the maximum load is reached, a nonlinear behaviour can be seen, which means that the interface is now developing the C and/or S stages within a bonded area close to the CFRP-loaded end. Although specimen A200-AD has a higher η value than specimen A180-AD, the former developed a short plateau at the maximum value. The post-peak behaviour is also well predicted by the proposed FDM. However, it should be noted that the differences observed during the post-peak behaviour are due to the bond-slip relationship adopted in both works. If the bond-slip relationship has a finite final slip (often denoted as s_f in the literature, e.g. [39,92–95]) the complete debonding of the CFRP-to-steel joint, i.e. with no load transmitted to the CFRP composite, will occur at that value. Otherwise, the loads will increase once again to infinite slip and zero load transmitted to the CFRP composite as previously documented in the literature by the authors [69].

The IAE values calculated according to Eq. (36) also confirm the accuracy of the proposed FDM. Thus, in both specimens, the calculated IAE values were similar and approximately equal to 3.5 % until the occurrence of the snap-back. However, considering the full debonding process, IAE values of approximately 6.5 % and 6.1 % in specimens A180-AD and A200-AD were calculated, respectively. These results confirm, therefore, the FDM high level of accuracy in predicting the influence of multiple debonding defects on CFRP-to-steel single-lap tests.

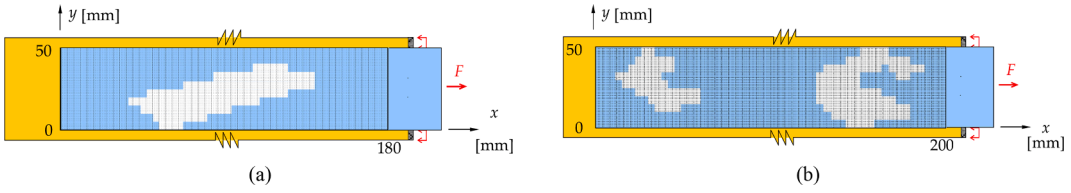

Fig. 12. Geometry of the debonding defects the specimens tested by Wang et al. [87] with a bonded length of: (a) 180 mm – A180-AD; (b) 200 mm – A200-AD.

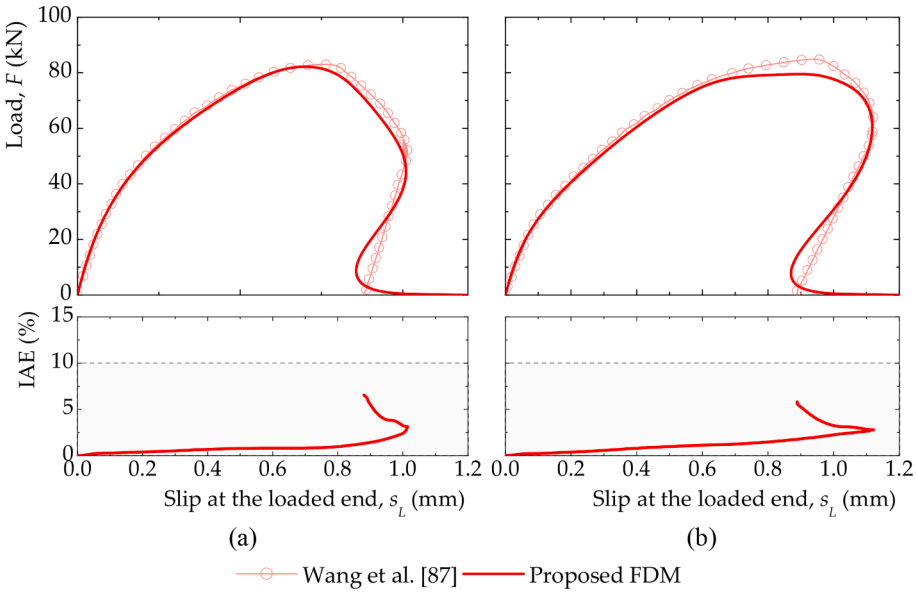

Fig. 14. Precision of the proposed FDM in the determination of the load vs. slip at the loaded end curves of the specimens by Wang et al. [87] with: (a) $L_b = 180$ mm and $\eta \approx 28.0$ %; and (b) $L_b = 200$ mm and $\eta \approx 37.2$ %.

6. Conclusions

This work aimed to propose a new numerical strategy that could facilitate the comprehension and interpretation of the influence of multiple debonding defects on CFRP-to-steel bonded joints. To that end, the FDM was implemented and to give a wider perspective of such influence on CFRP-to-steel joints, brittle and ductile adhesives were considered. Moreover, a new single-function bond-slip relationship was proposed and implemented in the FDM, which allowed for describing the local bond behaviour of the joints with a brittle or ductile adhesive through the same local adherence model. A total of 56 different specimens (a total of 112 different models), were simulated by the proposed FDM and the results were compared either with the FEM or with another study available in the literature [87]. Thus, based on the results obtained in the present work, the main conclusions are pointed out as follows:

- Since the calibration of the bond-slip relationships are not affected by the localized or dispersed debonding defects, the CFRP-to-steel joints with short bonded lengths did not change the shape of the local adhesion. Thus, for the approximation carried out in this work, the specimens with a brittle adhesive continued to reproduce an almost triangular shape characterized by an ascending branch and followed by another descending branch until full debonding of the specimens. On the other hand, the specimens with a ductile adhesive continued to show a *quasi*-trapezoidal shape characterized by four different branches: an initial and ascending, a constant, a descending and a debonding branch;
- Regarding the influence of localized or dispersed debonding defects on specimens with a short bonded length, it can be concluded that no significant influences can be obtained on the maximum loads reached. However, when compared with the reference specimens, the load degradations did not exceed 40 % at the highest η value of 75 % considered for these specimens;
- Depending on whether a brittle or ductile adhesive was used, the specimens with the longest bonded lengths have different load-slip curves. The specimens with a brittle adhesive showed a snap-through phenomenon, which is explained by the stress transfer between the first bonded region and the second one through the localized debonded region. Hence, unlike the reference specimens that have a plateau at maximum load, these joints show a load decrease followed by another load increase. After that, as the loads decreased once again, a snap-back phenomenon was observed. The snap-through phenomenon is barely observed in the specimens with the dispersed debonding, regardless of using a brittle or a ductile adhesive;
- Unlike the dispersed debonding defects, which had a major impact on the load capacity of joints with the longest bonded lengths, the localized debonding defect has much less impact on the maximum loads of the bonded joints, independently of the η value;
- Regardless of the debonding defect type, the ductility of the specimens, mainly in those with the longest bonded lengths, decreases with the increase of η. Despite being outside the scope of this work, debonding defects may have a severe impact on the bond behaviour when subject to cyclic loading and this requires therefore, further investigation in the future;
- The IAE parameter was chosen to assess the precision of the proposed FDM model when compared with the FEM. Thus, the highest IAE values were obtained in the specimens with the shortest bonded length with a brittle adhesive, where values between 10 and 15 % were obtained. Nevertheless, IAE values lower than 10 % were always obtained in the other cases, which shows the high accuracy obtained by the proposed FDM;
- The proposed FDM was also able to accurately replicate the bond behaviour of other specimens available in the literature [86]. In such cases, IAE values lower than 3.5 % were determined, which also shows the versatility of the proposed FDM.

Finally, it should be recognized that many other debonding defects could be generated as well as other definitions of the bond-slip relationships, different materials and/or geometries. However, for simplicity, the debonding defects and the CFRP-to-steel bonded joints were randomly selected and, therefore, it would be expected that the proposed FDM could reach similar levels of accuracy in other situations not reported in this study. Still, the proposed FDM has proven to have great potential for predicting the influence of multiple debonding defects in adhesively bonded structures subjected to a monotonic load. Therefore, the current work has contributed to the very first steps towards the comprehension of the influence of multiple debonding defects on CFRP-to-steel joints. A few research directions ahead can include the study of the bond performance of mechanically anchorage CFRP-to-steel joints or other bonded joints with other geometries (e.g. stepped joints, double strap joints, etc.) or subjected to other test conditions (e.g.

temperature variations or test setup configuration), and also the development of 3D models such that the proposed FDM could be compared with.

CRediT authorship contribution statement

Hugo C. Biscaia: Writing – review & editing, Writing – original draft, Validation, Software, Project administration, Methodology, Investigation, Funding acquisition, Formal analysis, Data curation. **Pedro Coelho:** Writing – review & editing, Resources, Investigation, Funding acquisition. **Fábio Conde:** Writing – review & editing, Investigation, Funding acquisition. **Tommaso D'Antino:** Writing – review & editing, Validation, Investigation, Formal analysis.

Declaration of competing interest

The authors declare the following financial interests/personal relationships which may be considered as potential competing interests: [Hugo C. Biscaia, Pedro Coelho and Fábio Conde report financial support was provided by Foundation for Science and Technology. Tomasso D'Antino reports no financial support of any kind.].

Data availability

Data will be made available on request.

Acknowledgments

The authors are thankful to Fundação para a Ciência e Tecnologia (FCT-MCTES) for the partial funding of this work under the strategic projects UIDP/00667/2020 and UIDB/00667/2020 and exploratory project EXPL/EME-APL/0994/2021.

References

[1] Chen JF, Teng JG. Anchorage strength models for FRP and steel plates bonded to concrete. J Struct Eng 2001;127(7):784–91.
[2] Silva MAG, Biscaia HC. Effects of exposure to saline humidity on bond between GFRP and concrete. Compos Struct 2010;93(1):216–24.
[3] Zaman A, Gutub SA, Wafa MW. A review on FRP composites applications and durability concerns in the construction sector. J Reinf Plast Compos 2013;32(24):1966–88.
[4] Heshmati M, Haghani R, Al-Emrani M. Environmental durability of adhesively bonded FRP/steel joints in civil engineering applications: State of the art. Compos B Eng 2015;81:259–75.
[5] Colombi P, Fava G. Fatigue crack growth in steel beams strengthened by CFRP strips. Theor. Appl. Fract. Mech. 2016;85(B):173–82.
[6] Chen T, Huang C, Hu L, Song X. Experimental study on mixed-mode fatigue behavior of center cracked steel plates repaired with CFRP materials. Thin-Walled Struct 2019;135:486–93.
[7] Silva MAG, Biscaia H, Ribeiro P. On factors affecting CFRP-steel bonded joints. Constr Build Mater 2019;226:360–75.
[8] Mensah C, Min B, Bonsu AO, Wang Z. Investigating the effect of steel fiber content on bond behavior between externally bonded CFRP-to-concrete joints. Structures 2022;36:565–79.
[9] Zhou Y, Chen X, Fan Z, Sui L, Li D, Xing F. Bond behaviors of FRP-to-concrete interface under the control of a novel end-anchorage system. Compos Struct 2017;168:130–42.
[10] Barris C, Correia L, Sena-Cruz J. Experimental study on the bond behaviour of a transversely compressed mechanical anchorage system for externally bonded reinforcement. Compos Struct 2018;200:217–28.
[11] Zhang W, Jia L, Luo K, Teng X. A novel anchor method for large tonnage CFRP cable: anchorage design and full-scale experiment. Compos Struct 2024;336:118004.
[12] Biscaia HC, Micaelo R, Chastre C. Cyclic performance of adhesively bonded joints using the Distinct Element Method: Damage and parametric analysis. Compos B Eng 2019;178:107468.
[13] Biscaia H, Micaelo R. Emerging anchored FRP systems bonded to steel subjected to monotonic and cyclic loading: a numerical study. Eng Fract Mech 2022;261:108250.
[14] Li Y, Mei K, Wang Y, Jia W, Sun S. Finite element model analysis of long-term performance of composite anchorage based on double-material parameters. J Build Eng 2024;87:109059.
[15] Diab HM, Farghal OA. Bond strength and effective bond length of FRP sheets/plates bonded to concrete considering the type of adhesive layer. Compos B Eng 2014;58:618–24.
[16] Biscaia HC, Silva MAG, Chastre C. Factors influencing the performance of externally bonded reinforcement systems of GFRP-to-concrete interfaces. Mater Struct 2015;48(9):2961–81.
[17] Li A, Wang H, Li H, Kong D, Xu S. Estimation of bond strength and effective bond length for the double strap joint between Carbon Fiber Reinforced Polymer (CFRP) plate and corroded steel plate. Polymers 2022;14(15):3069.
[18] Omairey S, Jayasree N, Kazilas M. Defects and uncertainties of adhesively bonded composite joints. SN Appl Sci 2021;3:769.
[19] Qiu C, Feng P, Yang Y, Zhu L, Bai Y. Joint capacity of bonded sleeve connections for tubular fibre reinforced polymer members. Compos Struct 2017;163:267–79.
[20] Yang X, Bai Y, Luo FJ, Zhao XL, He XH. Fiber-reinforced polymer composite members with adhesive bonded sleeve joints for space frame structures. J Mater Civ Eng 2017;29(2):04016208.
[21] Rajak DK, Wagh PH, Kumar A, Sanjay MR, Siengchin S, Khan A, et al. Impact of fiber reinforced polymer composites on structural joints of tubular sections: a review. Thin-Walled Struct 2022;180:109967.
[22] Biscaia H, Carvalho M, Martins AP, Micaelo R. Interfacial failure of circular or tubular hybrid bonded joints: a theoretical description. Eng Fail Anal 2022;132:105936.
[23] De Lorenzis L, Zavarise G. Interfacial stress analysis and prediction of debonding for a thin plate bonded to a curved substrate. Int J Non Linear Mech 2009;44:358–70.
[24] Basilio I, Fedele R, Lourenço PB, Milani G. Assessment of curved FRP-reinforced masonry prisms: experiments and modelling. Constr Build Mater 2014;51:492–505.
[25] Biscaia H, Chastre C, Silva MAG. Analytical model with uncoupled adhesion laws for the bond failure prediction of curved FRP-concrete joints subjected to temperature. Theor Appl Fract Mech 2017;89:63–78.
[26] Yuan Y, Milani G. Closed-form model for curved brittle substrates reinforced with FRP strips. Compos Struct 2023;304(1):116443.
[27] Wu C, Chen C, He L, Yan W. Comparison on damage tolerance of scarf and stepped-lap bonded composite joints under quasi-static loading. Compos B Eng 2018;155:19–30.
[28] Biscaia HC, Micaelo R, Cornetti P, Almeida R. Numerical bond assessment of carbon-epoxy stepped-lap joints. Eng Fract Mech 2023;289:109413.
[29] Demiral M, Mamedov A. Fatigue performance of a step-lap joint under tensile load: a numerical study. Polymers 2023;15(8):1949.
[30] Li PD, Zhao Y, Wu YF, Lin JP. Effect of defects in adhesive layer on the interfacial bond behaviors of externally bonded CFRP-to-concrete joints. Eng Struct 2023;278:115495.
[31] Wan B, Jiang C, Wu YF. Effect of defects in externally bonded FRP reinforced concrete. Constr Build Mater 2018;172:63–76.
[32] Kim SJ, Smith ST, Young B. Effect of Surface Preparation on the Strength of FRP-to-Mild Steel and FRP-to-Stainless Steel Joints. In: Ye L, Feng P, Yue Q, editors. Advances in FRP Composites in Civil Engineering. Heidelberg: Springer, Berlin; 2011.
[33] Fernando D, Teng JG, Yu T, Zhao XL. Preparation and characterization of steel surfaces for adhesive bonding. J Compos Constr 2013;17(6):04013012.
[34] Carnes MD, Mtenga PV. The effect of materials and surface preparation on joining methods: a review. J Reinf Plast Compos 2015;34(14):1167–78.
[35] Yang Y, Biscaia H, Silva MAG, Chastre C. Monotonic and quasi-static cyclic bond response of CFRP-to-steel joints after salt fog exposure. Compos B Eng 2019;168:532–49.
[36] Pang Y, Wu G, Wang H, Gao D, Zhang P. Bond-slip model of the CFRP-steel interface with the CFRP delamination failure. Compos Struct 2021;256:113015.
[37] Altaee JM, Altayee SAS, Kadhim MMA, Jawdhari A, Majdi A, Chabuk A, et al. Evaluation of existing bond-slip relations for CFRP-steel joints and new model for linear and nonlinear adhesives. Advances in Civil Engineering 2022;2022:3673438.
[38] Guo X, Wu Z, Yang Y, Bai J, Zhou Q. A study on the bond-slip relationship of the CFRP-steel interface of CFRP strengthened steel. Materials 2022;15(12):4187.
[39] Fernando D, Yu T, Teng JG. Behavior of CFRP laminates bonded to a steel substrate using a ductile adhesive. J Compos Constr 2014;18(2):04013040.
[40] He J, Xian G, Zhang YX. Numerical modelling of bond behaviour between steel and CFRP laminates with a ductile adhesive. Int J Adhes Adhes 2021;104:102753.
[41] Zhao J, Fang J, Yang Y, Zhang S, Biscaia H. Experimental study on mixed mode-I & II bond behavior of CFRP-to-steel joints with a ductile adhesive. Thin-Walled Struct 2023;184:110532.
[42] Biscaia HC, Chastre C, Viegas A. A new discrete method to model unidirectional FRP-to-parent material bonded joints subjected to mechanical loads. Compos Struct 2015;121:280–95.
[43] Zhao XL, Zhang L. State-of-the-art review on FRP strengthened steel structures. Eng Struct 2007;29(8):1808–23.
[44] Akbar I, Oehlers DJ, Ali MSM. Derivation of the bond–slip characteristics for FRP plated steel members. J Constr Steel Res 2010;66(8–9):1047–56.
[45] Fawzia S, Zhao XL, Al-Mahaidi R. Bond-slip models for double strap joints strengthened by CFRP. Compos Struct 2010;92(9):2137–45.
[46] Wang HT, Wu G, Dai YT, He XY. Determination of the bond–slip behavior of CFRP-to-steel bonded interfaces using digital image correlation. J Reinf Plast Compos 2016;35(18):1353–67.
[47] He J, Xian G. Debonding of CFRP-to-steel joints with CFRP delamination. Compos Struct 2016;153:12–20.

[48] Wang HT, Wu G. Bond-slip models for CFRP plates externally bonded to steel substrates. Compos Struct 2018;184:1204–14.
[49] Doroudi Y, Fernando D, Zhou H, Nguyen VT, Ghafoori E. Fatigue behavior of FRP-to-steel bonded interface: an experimental study with a damage plasticity model. Int J Fatigue 2020;139:105785.
[50] Yuan H, Teng JG, Seracino R, Wu ZS, Yao J. Full-range behavior of FRP-to-concrete bonded joints. Eng Struct 2004;26(5,):553–565.
[51] Caggiano A, Martinelli E, Faella C. A fully-analytical approach for modelling the response of FRP plates bonded to a brittle substrate. Int J Solids Struct 2012;49 (17):2291–300.
[52] Gao WY, Dai JG, Teng JG. Analysis of Mode II debonding behavior of fiber-reinforced polymer-to-substrate bonded joints subjected to combined thermal and mechanical loading. Eng Fract Mech 2015;136:241–64.
[53] Yang Y, Biscaia H, Chastre C, Silva MAG. Bond characteristics of CFRP-to-steel joints. J Constr Steel Res 2017;138:401–19.
[54] Nelson LA, Al-Allaf M, Weekes L. Analytical modelling of bond-slip failure between epoxy bonded FRP and concrete substrate. Compos Struct 2020;251:112596.
[55] Milani G, Grande E, Bertolesi E, Rotunno T, Fagone M. Debonding mechanism of FRP strengthened flat surfaces: analytical approach and closed form solution. Constr Build Mater 2021;302:124144.
[56] Biscaia HC, Chastre C, Borba IS, Silva C, Cruz D. Experimental evaluation of bonding between CFRP laminates and different structural materials. J Compos Constr 2016;20(3):04015070.
[57] Biscaia H, Chastre C. Design method and verification of steel plate anchorages for FRP-to-concrete bonded interfaces. Compos Struct 2018;192:52–66.
[58] Baena M, Torres L, Turon A, Barris C. Experimental study of bond behaviour between concrete and FRP bars using a pull-out test. Compos B Eng 2009;40(8): 784–97.
[59] Zhang P, Zhang S, Gao D, Dong F, Liu Y, Zhao J, et al. Influence of rib parameters on mechanical properties and bond behavior in concrete of fiber-reinforced polymer rebar. Adv Struct Eng 2021;24(1):196–208.
[60] Shen D, Ojha B, Shi X, Zhang H, Shen J. Bond stress-slip relationship between basalt fiber-reinforced polymer bars and concrete using a pull-out test. J Reinf Plast Compos 2016;35(9):747–63.
[61] Liu X, Wang X, Xie K, Wu Z, Li F. Bond behavior of basalt fiber-reinforced polymer bars embedded in concrete under mono-tensile and cyclic loads. Int J Concrete Struct Mater 2020;14:19.
[62] Huang L, Chen J, Qu J, Dai Q. Modeling for bond-constitutive relationships of FRP rebars to concrete matrix. Constr Build Mater 2020;263:120654.
[63] Rolland A, Argoul P, Benzarti K, Quiertant M, Chataigner S, Khadour A. Analytical and numerical modeling of the bond behavior between FRP reinforcing bars and concrete. Constr Build Mater 2020;231:117160.
[64] Chaboche JL, Girard R, Schaff A. Numerical analysis of composite systems by using interphase/interface models. Comput Mech 1997;20(1–2):3–11.
[65] Lin G, Geubelle PH, Sottos NR. Simulation of fiber debonding with friction in a model composite pushout test. Int J Solids Struct 2001;38(46–47):8547–62.
[66] Wang Z, Li C, Sui L, Xian G. Effects of adhesive property and thickness on the bond performance between carbon fiber reinforced polymer laminate and steel. Thin-Walled Struct 2021;158:107176.
[67] Wang HT, Gang W, Dai YT, He XY. Experimental study on bond behavior between CFRP plates and steel substrates using digital image correlation. J Compos Constr 2016;20(6):04016054.
[68] Biscaia HC, Chastre C, Silva MAG. Bond-slip model for FRP-to-concrete bonded joints under external compression. Compos B Eng 2015;80:246–59.
[69] Biscaia HC, Borba IS, Silva C, Chastre C. A nonlinear analytical model to predict the full-range debonding process of FRP-to-parent material interfaces free of any mechanical anchorage devices. Compos Struct 2016;138:52–63.
[70] Calabrese AS, Colombi P, D'Antino T. Analytical solution of the bond behavior of FRCM composites using a rigid-softening cohesive material law. Compos B Eng 2019;174:107051.
[71] Carvalho T, Chastre C, Biscaia H, Paula R. Flexural behaviour of RC T-beams strengthened with different FRP materials. May-June: Third International fib Congress Washington; 2010.
[72] Dai JG, Ueda T, Sato Y. Unified analytical approaches for determining shear bond characteristics of FRP-concrete interfaces through pullout tests. J Adv Concr Technol 2006;4(1):133–45.
[73] Yang DS, Hong SN, Park SK. Experimental observation on bond-slip behavior between concrete and CFRP plate. Int J Concrete Struct Mater 2007;1(1):37–43.
[74] Biscaia H, Chastre C. Theoretical analysis of fracture in double overlap bonded joints with FRP composites and thin steel plates. Eng Fract Mech 2018;190:435–60.
[75] We H, Wang X, Ding L, Wu Z. Experimental study on bond behavior of interface between fiber-reinforced polymer grids and concrete substrate. Compos Struct 2021;257:113164.
[76] Biscaia HC, Chastre C, Silva MAG. A simple method for the determination of the bond-slip model of artificially aged joints. J Compos Constr 2019;23(4):04019028.
[77] Carrara P, Ferretti D, Freddi F, Rosati G. Shear tests of carbon fiber plates bonded to concrete with control of snap-back. Eng Fract Mech 2011;78(15):2663–78.
[78] Cornetti P, Carpinteri A. Modelling the FRP-concrete delamination by means of an exponential softening law. Eng Struct 2011;33(6):1988–2001.
[79] Yuan Y, Milani G. A simplified analytical model for FRP-strengthened curved brittle substrates using the multi-linear bond-slip law. Buildings 2023;13(10):2579.
[80] Rozylo P, Falkowicz K. Stability and failure analysis of compressed thin-walled composite structures with central cut-out, using three advanced independent damage models. Compos Struct 2021;273:114298.
[81] Yang Y, Zhao J, Zhang S, Chastre C, Biscaia H. Effect of mechanical anchorage on the bond performance of double overlapped CFRP-to-steel joints. Compos Struct 2021;267:113902.
[82] Rozylo P, Debski H. Failure study of compressed thin-walled composite columns with top-hat cross-section. Thin-Walled Struct 2022;180:109869.
[83] Rozylo P. Comparison of failure for thin-walled composite columns. Materials 2022;15(1):167.
[84] Cervenka V, Jendele L, Cervenka J. ATENA Program Documentation – Part 1 – Theory. Prague: Cervenka Consulting; March 2021.
[85] Biscaia H. The influence of temperature variations on adhesively bonded structures: a non-linear theoretical perspective. Int J Non Linear Mech 2019;113: 67–85.
[86] Biscaia HC. Closed-form solutions for modelling the response of adhesively bonded joints under thermal loading through exponential softening laws. Mech Mater 2020;148:103527.
[87] Wang G, Chen T, Cao C, Zheng Y. Strip-based numerical analysis of CFRP-reinforced steel plates with multiple debonding defects using the Runge-Kutta method. Compos Struct 2024;337:118059.
[88] Wu YF, Zhao XM. Unified bond stress-slip model for reinforced concrete. J Struct Eng 2013;139(11):1951–62.
[89] Shen D, Shi X, Ji Y, Yin F. Strain rate effect on bond stress-slip relationship between basalt fiber-reinforced polymer sheet and concrete. J Reinf Plast Compos 2015;34 (7):547–63.
[90] Biscaia H, Almeida R, Zhang S, Canejo J. Experimental calibration of the bond-slip relationship of different CFRP-to-timber joints through digital image correlation measurements. Compos Part C: Open Access 2021;4:100099.
[91] Täljsten B. Defining anchor lengths of steel and CFRP plates bonded to concrete. Int J Adhes Adhes 1997;17(4):319–27.
[92] Teng JG, Smith ST, Chen JF. Flexural strengthening of reinforced concrete (RC) beams with fibre-reinforced polymer (FRP) composites. In: Strengthening and Rehabilitation of Civil Infrastructures Using Fibre-Reinforced Polymer (FRP) Composites. Woodhead Publishing Series in Civil and Structural Engineering, 2008:112-140.
[93] Jiang C, Yun QQ, Gu XL. A unified bond-slip model for the interface between FRP and steel. Compos B Eng 2021;227:109380.
[94] Xia SH, Teng JG. Behaviour of FRP-to-steel bonded joints. In: Proceedings of international symposium on bond behavior of FRP in structures. International Institute for FRP in Construction, Hong Kong, 2005, pp. 411-418.
[95] Calabrese AS, Colombi P, D'Antino T. Analytical solution of the full-range behavior of adhesively bonded FRP-steel joints made with toughened adhesives. Eng Fract Mech 2023;292:109569.